Long-term implant fibrosis prevention in rodents and non-human primates using crystallized drug formulations

Shady Farah[1,2,3,13], Joshua C. Doloff [1,2,3,12,13], Peter Müller[4], Atieh Sadraei [1], Hye Jung Han[1,3], Katy Olafson[1,2,3,5], Keval Vyas[1], Hok Hei Tam[1,3], Jennifer Hollister-Lock[6], Piotr S. Kowalski[1,2], Marissa Griffin[1], Ashley Meng[1], Malia McAvoy[1,7], Adam C. Graham[8], James McGarrigle[9], Jose Oberholzer[9], Gordon C. Weir[6], Dale L. Greiner[10], Robert Langer[1,2,3,7,11] and Daniel G. Anderson[1,2,3,7,11]*

Implantable medical devices have revolutionized modern medicine. However, immune-mediated foreign body response (FBR) to the materials of these devices can limit their function or even induce failure. Here we describe long-term controlled-release formulations for local anti-inflammatory release through the development of compact, solvent-free crystals. The compact lattice structure of these crystals allows for very slow, surface dissolution and high drug density. These formulations suppress FBR in both rodents and non-human primates for at least 1.3 years and 6 months, respectively. Formulations inhibited fibrosis across multiple implant sites—subcutaneous, intraperitoneal and intramuscular. In particular, incorporation of GW2580, a colony stimulating factor 1 receptor inhibitor, into a range of devices, including human islet microencapsulation systems, electrode-based continuous glucose-sensing monitors and muscle-stimulating devices, inhibits fibrosis, thereby allowing for extended function. We believe that local, long-term controlled release with the crystal formulations described here enhances and extends function in a range of medical devices and provides a generalized solution to the local immune response to implanted biomaterials.

mplanted biomedical devices are an integral part of modern therapeutics, playing key roles in many clinical applications including neural interfacing[1], monitoring vital signs[2], pacemakers[3], controlled drug release[4], scaffolds for tissue reconstruction[5], vascular stenting, cell encapsulation and transplantation[6]. While the immunological response to materials can be therapeutic, for example, with particulate vaccines[7], some device materials, including polysaccharides, polymers, ceramics and metals[8], can induce host immune-mediated foreign body and rejection responses. These responses can lead to fibrotic encapsulation, and in some cases, reduced efficacy or failure[8–12]. Current approaches for long-term maintenance of biomedical device implant biocompatibility often involve broad-spectrum anti-inflammatories[13]. Short-term steroid or anti-fibrotic drug delivery can transiently inhibit inflammatory cell recruitment as well as improve protein secretion of immuno-isolated cellular grafts[14,15]. However, many anti-inflammatory drugs have multiple targets and differential effects in vivo, and associated toxicity[13,16]. In particular, macrophages are known to be key mediators of the immune response to implanted biomaterials[8–10]. Recently, it has been shown that the implant-induced foreign body response (FBR) can be inhibited through selective targeting of the monocyte/macrophage-expressed colony stimulating factor 1 receptor

(CSF1R)[10]. Importantly, while macrophage numbers in the intraperitoneal space as well as other essential macrophage functions, such as vascular endothelial growth factor production, wound healing and phagocytosis, are found to be left intact[10], cellular phenotype is different at the level of both RNA (gene expression) and protein (fluorescence-activated cell sorting (FACS)), indicating a shift in macrophage behaviour. Inhibition of CSF1R has also previously been shown to induce macrophage polarization[17].

Systemic application of broad-spectrum non-steroidal anti-inflammatories has been associated with hepatocellular, cardiac or renal toxicities[18], gastrointestinal ulceration bleeding and microbial dysbiosis[19]. Specific inhibitors of molecular targets implicated in macrophage response can have side effects when dosed globally. For example, tumour-necrosis factor-α (TNF-α) inhibitors can increase infection occurrence and risks of autoimmunity, and worsen neurologic and/or congestive heart failure prognosis[20]. Anti-transforming growth factor-β compounds can increase risks of autoimmunity and cancer (keratoacanthomas)[21], and those against CSF1R receptor can elicit fatigue/asthenia, edema and assorted other side effects[17]. Given that there are macrophage populations in every major tissue of the body[22], we sought to develop a long-lasting, localized delivery system. Locally releasing, drug-eluting devices

---

[1]David H. Koch Institute for Integrative Cancer Research, Massachusetts Institute of Technology, Cambridge, MA, USA. [2]Department of Chemical Engineering, Massachusetts Institute of Technology, Cambridge, MA, USA. [3]Department of Anesthesiology, Boston Children's Hospital, Harvard Medical School, Boston, MA, USA. [4]X-Ray Diffraction Facility, MIT Department of Chemistry, Massachusetts Institute of Technology, Cambridge, MA, USA. [5]Department of Chemical and Biomolecular Engineering, University of Houston, Houston, TX, USA. [6]Section on Islet Cell and Regenerative Biology, Research Division, Joslin Diabetes Center, Boston, MA, USA. [7]Harvard-MIT Division of Health Science Technology, Massachusetts Institute of Technology, Cambridge, MA, USA. [8]Center for Nanoscale Systems, Harvard University, Cambridge, MA, USA. [9]Department of Surgery, Division of Transplantation, University of Illinois at Chicago, Chicago, IL, USA. [10]Program in Molecular Medicine, University of Massachusetts Medical School, Worcester, MA, USA. [11]Institute for Medical Engineering and Science, Massachusetts Institute of Technology, Cambridge, MA, USA. [12]Present address: Department of Biomedical and Materials Science Engineering, Translational Tissue Engineering Center, Wilmer Eye Institute and the Institute for NanoBioTechnology, Johns Hopkins University School of Medicine, Baltimore, MD, USA. [13]These authors contributed equally: Shady Farah, Joshua C. Doloff. *e-mail: dgander@mit.edu

have shown utility in increasing treatment specificity and reducing off-target effects associated with systemic administration[23]. For example, local controlled release of glucocorticoids and anti-proliferative drugs has been shown to reduce fibroblast proliferation and collagen deposition on pacemaker leads[24], stents, vascular grafts and biosensors[25,26]. Dexamethasone released from electrospun fibres[27] and drug-eluting sutures[28] decreases the FBR and host rejection of biomaterials for various medical applications. Ketoprofen release from selectively permeable, porous microcapsules reduced post-transplant acute inflammation[29], and corticosteroid stabilized in viscous polymers has also yielded improved anti-inflammatory release[30]. However, despite improvements with locally integrated elution systems, the duration of many release strategies is limited to around 30–60 d, with the lack of longevity resulting in a delay with eventual resumption of immune and fibrosis responses once lingering effects of inhibition are lost[31]. Complicating factors include constant macrophage replenishment in the body[32] as well as the ability of macrophages to shift phenotype once the local microenvironment reverts to an untreated state[33]. As such, attempts to prevent implant rejection long term, or utilize anti-inflammatory drugs for long-term cell-based therapeutics, have remained challenging.

Controlled drug delivery through microencapsulation has been broadly explored, and typically involves an encapsulation material or device[34]. However, these devices are often made of materials that can themselves induce inflammation[6,35]. Furthermore, microencapsulation typically results in a device that is composed primarily of the encapsulation material, not the drug, limiting the amount of drug that can be included for a given volume[34]. Finally, there are many devices where function is desired for very long time periods, on the order of years, requiring the development of a very slow and compact drug-releasing system[1–6]. We sought to address these challenges through the development of a controlled drug delivery system based on drug crystal formation. Crystallization has largely been utilized to image essential protein folding and observe target–agent interactions[36], or, in more industrial fields, for purification purposes[37]. Crystallized drug formulations for controlled drug release have been described in the literature; however, they have typically been used as nano- to few micrometre surface coatings[38,39] or in carrier-based formulations with low encapsulation efficiencies and limited release duration from hours to weeks[40,41]. Crystalline materials have also exhibited advantages of enhanced chemical stability[42].

In the area of drug delivery, given that many CSF1R inhibitors and broad-spectrum anti-inflammatory agents are highly hydrophobic, creating difficulties for pharmacologists to solubilize and formulate them for delivery in non-toxic ways[43], we felt that utilization of such a strategy would enable large concentrated, pure drug reservoirs to be delivered in a highly localized manner for long-term release. Herein, we report the development of compact solvent-free crystalline anti-fibrotic drug formulations for localized long-term delivery. These crystal formulations were shown to enable long-term function in the absence of fibrosis in a range of devices, including alginate encapsulated cells, electrode-based continuous glucose-sensing monitors (CGMs) and muscle-stimulating devices (MSDs). Long-term anti-fibrotic efficacy and implant utility were maintained across multiple implant sites—subcutaneous (SC), intraperitoneal (IP) and intramuscular (IM). These studies were performed in a range of animals, including SKH1 mice (SC), healthy and diabetic (streptozotocin (STZ) treated) C57BL/6 mice (IP and SC), Sprague–Dawley rats (IM) and non-human primate (NHP) cynomolgus monkeys (IP and SC). Initial studies were performed using rodent strains that had previously been investigated as model systems for fibrosis[10–12], and further validated in NHPs.

Macrophage-targeted agents with anti-fibrotic activity
From the literature, we identified 12 immunomodulating drugs with either known history or the potential to block fibrosis

locally[10,14,23,24,27,44,45]. This list included some broad-spectrum anti-inflammatories, as well as agents targeted to essential macrophage biology pathways (Fig. 1). To investigate the effect of macrophage immunomodulation on FBR, we fabricated Ba^{2+}-cross-linked SLG20 alginate hydrogel spheres with these drugs, prepared as amorphous formulations (Supplementary Fig. 1a). Drug-containing spheres (500 µl per animal) were then implanted into the IP space (relevant for encapsulated islet biomass transplantation or placement of devices such as ports, catheters/cannulas and meshes) of C57BL/6 mice ($n = 5$ per group) for 14 d. Afterwards, spheres were retrieved and analysed for cellular deposition and fibrosis (Fig. 1 and Supplementary Fig. 1b,c). Dark-field phase-contrast images from collected spheres showed a marked reduction in cellular deposition on spheres in numerous drug groups (Fig. 1a and Supplementary Fig. 1b). This deposition on spheres was examined further with confocal microscopy for 4,6-diamidino-2-phenylindole (DAPI; nucleus marker), F-actin (cellular cytoskeleton marker) or macrophage marker CD68, and alpha-smooth muscle actin (α-SMact; myofibroblast marker) (Fig. 1a and Supplementary Fig. 1c).

Macrophage cell phenotype can be characterized through gene expression analysis of factors that correlate with macrophage activation[46]. To better understand macrophage responses as a function of different amorphous drug encapsulated within implanted alginate spheres, we used NanoString multiplexed gene expression analysis to profile host-mediated innate immune recognition following 14 d of implantation (Fig. 1b). Fibrosis-associated macrophage phenotypes and corresponding fibrotic response correlated as numerous drugs inhibited host response to varying degrees (Fig. 1b, green), compared with no drug (blank) and vehicle-loaded (dimethyl sulfoxide (DMSO)) controls. Inhibitors with similar targets induced similar phenotypes and most showed significant reduction of inflammatory macrophage markers sphingosine kinase 1 (Sphk1), TNF-α, arginase 1 (Arg1) and interleukin-1 (IL-1)[33,46]. Activated myofibroblast marker α-SMact and fibrosis marker collagen 1a1 (Col1a1) were also decreased on the surface of numerous drug-encapsulating hydrogel implants, in a similar fashion, compared with fibrosed controls. Corroborating observed decreases in expression of macrophage marker CD68 on drug-eluting capsules, flow cytometry confirmed significant decreases in adherent macrophages and neutrophils (Fig. 1c), compared with those on no drug (blank, red) and DMSO vehicle (black) implants. Remaining drug extracted from retrieved capsules indicated less than 5% was found attributing the observed activity to the vast majority of payload release (Fig. 1d). The pharmacological agents with the highest anti-fibrotic efficacy, including CC-5013, dexamethasone, QNZ, Ly2157299, curcumin, Ki20227 and GW2580, were chosen as a focus for the development of long-releasing formulations.

Design of drug formulations for long-term release
To enable long-term anti-fibrotic function in vivo, we sought to develop compact crystal formulations to allow long-term, controlled release with high drug density (Fig. 2a). Various techniques have been reported in the literature for compound crystallization, including the use of additives and co-crystals[39]. Here, we examined three different techniques to induce crystallization using GW2580 as a model compound: (1) solvent evaporation-induced crystallization (MI), (2) temperature-induced crystallization (MII) and (3) crystallization in solvent/anti-solvent mixture (MIII) (Supplementary Fig. 2). Solvent evaporation (MI) resulted in low reproducibility of crystal structure, including random crystallization and large fractions with twinning (Supplementary Figs. 2a and 3a). The second (temperature-induced) technique (MII) produced crystals with a wide size range as well as solvent molecules in their lattice (Fig. 2b and Supplementary Figs. 2a and 3b–d). Alternatively, a solvent/anti-solvent mixture of polar/non-polar solvents (MIII),
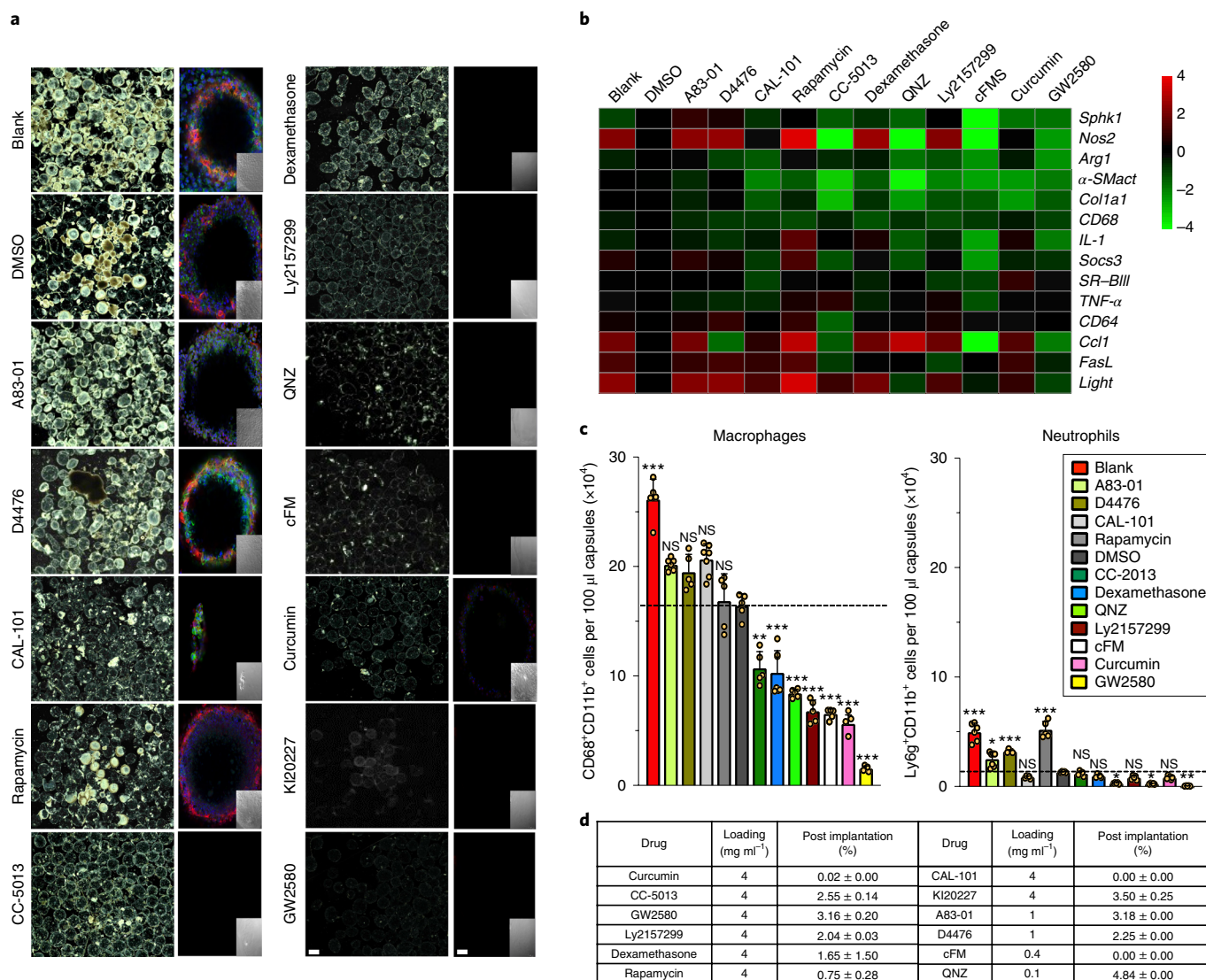
Fig. 1 | Anti-fibrotic drug screen testing agents largely targeted to macrophage biology. a, Phase-contrast (left) and confocal (right) images of capsules (blank, DMSO vehicle or containing amorphous drug, as indicated) retrieved following implantation into the IP space of C57BL/6 mice for two weeks. Phase-contrast images show host FBR immune cell adhesion and fibrosis. Confocal microscopy images show reduced or no fibrotic overgrowth on alginate microcapsules. Blue, DAPI nuclear stain; green, cellular cytoskeleton marker F-actin; red, fibrosis marker α-SMact. Insets: bright-field images of the same fields of view in the main confocal panel. Scale bars, 500 μm (phase contrast) and 50 μm (confocal). **b**, Multiplexed NanoString gene expression analysis of macrophage subtyping and fibrosis markers for RNA isolated from the surface of free-floating blank (no drug), drug vehicle (DMSO—for amorphous formulations) and amorphous drug-loaded microsphere capsules, following a two-week implantation in C57BL/6 mice. Interestingly, both cFMS receptor inhibitor III (cFMS) and GW2580 target CSF1R showed almost identical gene expression responses. Red, increase in expression; green, decrease in expression, compared with vehicle (DMSO) loaded. *Nos2*, nitric oxide synthase 2; *Socs3*, suppressor of cytokine signalling 3; *SR–BIII*, scavenger receptor class B type III; *Ccl1*, C-C motif chemokine ligand 1; *FasL*, Fas ligand. **c**, Quantitative FACS analysis of macrophages (left) and neutrophils (right) performed on cells dissociated directly off of alginate spheres. Some drugs significantly reduced macrophage and neutrophil presence. Data are mean ± s.e.m. The dashed line represents the level of response for vehicle (DMSO)-only control in Alginate. **d**, Table showing that all compounds, encapsulated in their amorphous form, either ran out or had less than 5% drug remaining after only a two-week IP implantation in C57BL/6 mice. Statistical analysis: one-way ANOVA plus Bonferroni multiple comparison correction; *$P < 0.05$; **$P < 0.001$; ***$P < 0.0001$; NS, not significantly different. For all in vivo data, $N = 5$ mice per group. All subpanels reflect representative data from in vivo experiments repeated three times.

specifically ethyl acetate/*n*-hexane was found to be a reproducible method for producing compact crystals with a more controlled range of crystal size and a crystalline lattice free of solvent (Fig. 2b and Supplementary Figs. 2 and 3b–e). A range of different parameters was explored, including drug concentration, solvent mixtures, processing time and temperature, to identify conditions that enabled a pure drug crystal formulation, with no additives and an ordered crystalline structure (Supplementary Fig. 4). Crystals from both techniques MII and MIII were found to behave differently

on contact with aqueous media, attributable to the differences in their crystalline lattice structure (that is, presence (MII) versus lack (MIII) of solvent) (Fig. 2c, Supplementary Figs. 2b and 3b–d, and Supplementary Video 1). MIII crystals were found to exhibit higher thermal stability than MII crystals as found by differential scanning calorimetry (DSC) and thermogravimetric analysis (TGA) (Supplementary Fig. 3e,f). A single sharp melting temperature peak was identified at 216.40 °C indicating a pure fraction of compact crystals, while MII crystals exhibited two peaks at 145 °C and 189 °C
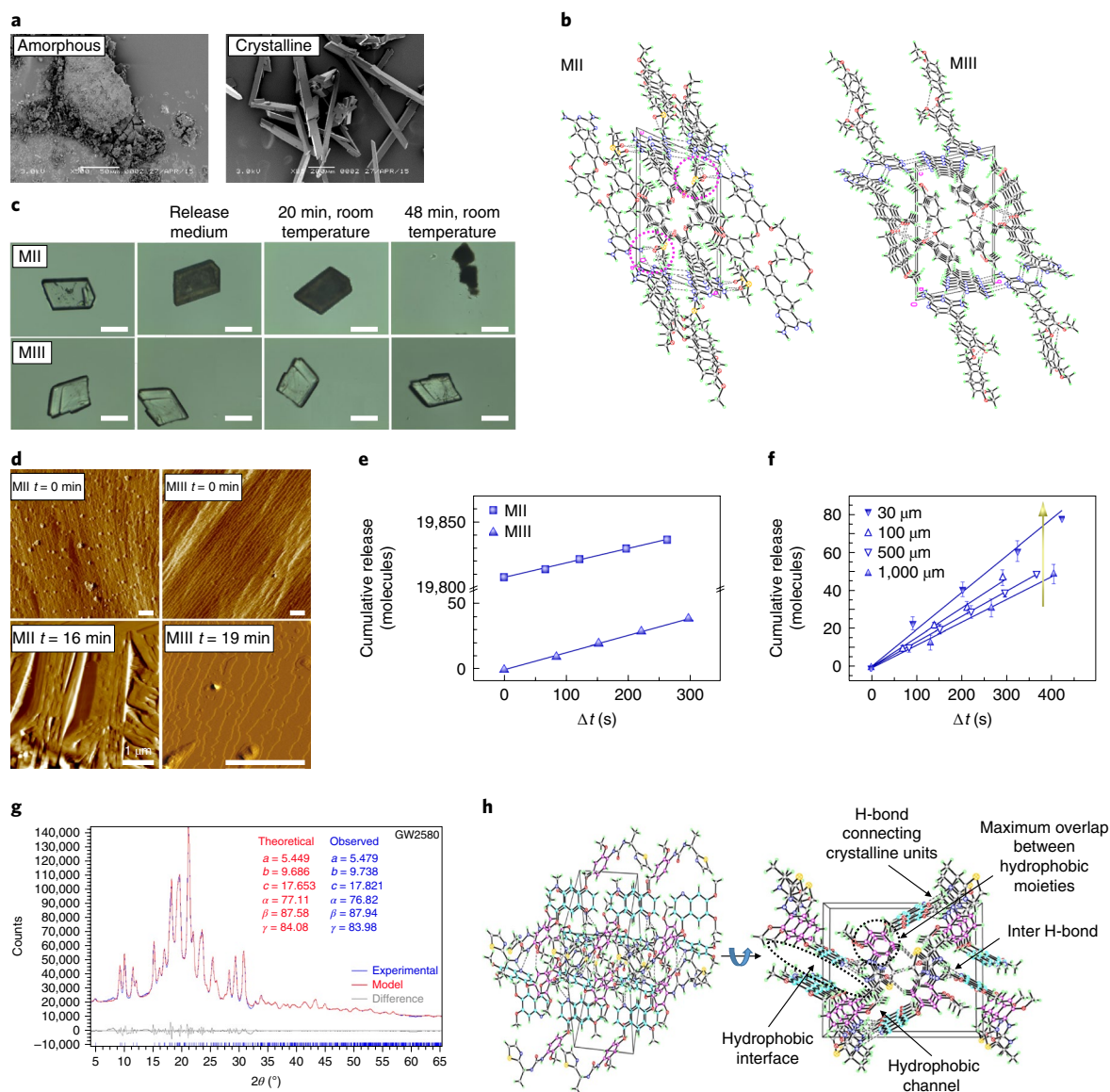
Fig. 2 | Crystal development and characterization. In depth comparison of crystal forms derived from different crystallization methods. **a**, Representative SEM images of fine amorphous and large crystals of the CSF1R inhibitor GW2580 (Supplementary Fig. 4b). **b**, Two representative examples of the three-dimensional packing pattern inside the GW2580 crystals developed by two crystallization methods, MII versus MIII, as revealed by SXRD, exhibiting solvent molecule inclusion/involvement inside the crystalline units (MII) versus solvent-free crystals (MIII). **c**, Microscope images showing the first contact of GW2580 crystals with aqueous medium (PBS). MII crystals turn from opaque to black due to fast release attributed to solvent-facilitated collapse, while MIII crystals exhibited slow surface release over the same period. Scale bars, 100 μm. **d**, Time-resolved in situ AFM showing real-time release from GW2580 crystal surfaces in a physiologically relevant environment (PBS, 37 °C). MII and MIII crystals were monitored at $t = 0$ min (open to air) and $t = 16$ min or 19 min, respectively (in solution). Scale bars, 1 μm. **e**, Cumulative molecules released from the surface of GW2580 crystals found by in situ AFM: MII versus MIII (same size). Time axis: $\Delta t = t - t_0$, where t is the time of image collection and t_0 is the elapsed time between addition of buffer and heating to 37 °C and the first dissolution measurement (Supplementary Fig. 5). Error bars are smaller than the symbol size. **f**, Cumulative molecules released from MIII crystals of different size, where $t_0 \approx 30$ s across all independent in situ AFM experiments. All line graph data are mean ± s.e.m. **g**, PXRD polymorph analysis (theoretical versus measured) of CSF1R inhibitor GW2580. **h**, Two representative SXRD crystal structures (different rotations of Ki20227) showing interaction (hydrophobic and hydrogen bonds) between the drug molecule's moieties inside the crystalline units as well as hydrogen bonds (semi-cross-linkers) between the repeating units. All subpanels reflect representative data from in vitro experimental analyses repeated three times.

attributed to DMSO followed by crystal collapse and melting[47,48] (Supplementary Discussion 1).

Determining the mechanism of drug release

Next, we aimed to examine drug release of GW2580 from crystals prepared by both techniques MII and MIII: crystal form 1 (F1) from MII and the highly compact crystal form 2 (F2) from MIII. Towards determining the different rates of release of drug forms F1

and F2, we employed in situ time-resolved atomic force microscopy (AFM) (Supplementary Fig. 5)[49]. This technique enabled us to monitor the real-time release of molecules from their crystal surfaces under physiological conditions. Crystals were placed in an undersaturated phosphate buffer (PBS) solution at 37 °C and sequential AFM images were collected. To compare release rates, we monitored the crystal surface for F2 (MIII) versus F1 (MII) (Fig. 2d,e and Supplementary Fig. 5), and for F2 (MIII) as a function of crystal size

(Fig. 2f). We identified significant differences in the mechanisms by which molecules are released from F1 and F2. On the (001) F2 crystal surface, we observed the formation of monomolecular height and larger (>10 nm) etch pits (Fig. 2d and Supplementary Fig. 5d). Overall, our in situ observations indicated that F2 crystals dissolve by surface dissolution and etch-pit expansion leading to slow surface release. In contrast, F1 crystals collapsed at the grain boundaries after immersion at 37 °C, resulting in a burst of drug release (Fig. 2c–e and Supplementary Figs. 2b and 5d). Following this initial collapse, F1 crystals were observed to dissolve from the edges of the grain boundaries and no single steps were observed on the (001) faces. Importantly, we noted that F2 crystals are stable during in situ conditions over extended time periods and can enable controlled release (Supplementary Discussion 2).

Identification of crystalline properties and polymorphism
Crystals developed by MIII were found to have uniform (single polymorph) repeating crystalline units as confirmed by powder X-ray diffraction (PXRD) and were found to be different from their amorphous form as shown by scanning electron microscopy (SEM) (Fig. 2a,g). In addition, a number of internal molecular interaction properties resulted from this formulation strategy, as confirmed by single-crystal X-ray diffraction (SXRD) (Fig. 2b). This method was also used to form compact crystals with drugs Ki20227, QNZ, dexamethasone, curcumin and CC-5013, which all have similar density, single polymorphism and crystalline packaging (Fig. 2h and Supplementary Figs. 6 and 7). This formulation methodology yielded higher-than-average crystal structure packing density with non-hydrogen atom volumes ranging from 15 to 18 $Å^3$ calculated by SXRD, compared with approximately 18 to 21 $Å^3$ for most of the pharmaceuticals[50,51]. We believe that these compact properties derive from prominent interaction interfaces between hydrophobic components inside the crystalline lattice and hydrogen bonding between crystalline repeating units.

Drug encapsulation and release rate
Crystals were mixed in alginate solution and then encapsulated using an electrospray gelation system as previously reported[11]. Flow rate, voltage and alginate concentration were optimized for uniform capsule formation as detailed in the Methods. First, we examined release as a function of the percentage of crystallinity in the capsules. Pure crystalline, amorphous or crystalline/amorphous mixtures were encapsulated and release was examined for two months (Supplementary Fig. 8). In another study, release was examined after encapsulation of pure crystal formulations with different size ranges, or as a mixture with amorphous drug, under accelerated release conditions (Fig. 3a,b and Supplementary Figs. 9 and 10a,b).

In general, controlling the ratio of drug form and crystal size or size range allowed for control of release rates.

Long-term anti-fibrotic effects of drugs in vivo
Leading drug candidates identified for their anti-fibrotic potential (Fig. 1) were crystallized, encapsulated in 500 μm alginate spheres and then implanted into the IP space of C57BL/6 mice for long-term testing (Fig. 3c–j). These capsules were retrieved after one, three and six months and analysed for cellular deposition and fibrosis. Interestingly, all capsules containing drug crystals were fibrosis free, as determined by phase-contrast imaging and confocal microscopy (Fig. 3c and Supplementary Fig. 10c,d). Control alginate spheres without drug exhibited fibrosis at one month and extensive clumping at three and six months post-implant (Fig. 3c). FACS analysis of cells isolated from retrieved capsules indicate reduced innate immune cell presence on the surfaces of retrieved crystalline drug-loaded capsule groups, even six months post-implantation (Fig. 3d and Supplementary Fig. 10e). Remaining drug crystals were found in retrieved capsules even after six months (Fig. 3e,i,j and Supplementary Fig. 11).

To confirm anti-fibrotic efficacy in another implant site, histological staining (Masson's trichrome and haematoxylin and eosin (H&E)) of capsules placed in the subcutaneous space revealed that capsules with drugs have significantly reduced cellular infiltration and fibrotic (collagen) deposition after three months (Fig. 3f). FACS analysis of cells taken from retrieved and dissociated SC tissues with capsules confirmed significantly reduced macrophage levels on and around implants (Fig. 3g). To determine whether fibrosis-free capsules were due to local or global immunomodulation, plasma drug concentrations were monitored throughout the study by liquid chromatography–mass spectrometry (LCMS). Interestingly, drug levels were below the reported drugs' half maximal inhibitory concentration (2.5–21 ng ml^{-1}) (Fig. 3h) and also below detection limits within one to two weeks post-implantation, depending on whether capsules were placed into IP or SC sites. This indicates that the observed anti-fibrotic effects are likely due to localized as opposed to systemic immunosuppression. Drug extraction analysis by high-performance liquid chromatography (HPLC) also determined that a notable percentage of the loaded drug, especially for SC samples, remained within explanted capsules (Fig. 3i,j), suggesting that fibrosis prevention could continue for a longer period of time.

Drug release and anti-fibrotic effects in NHPs
Next, we wanted to confirm whether these findings, which include multiple implant sites, could translate to a higher-order species. Leading drug GW2580 was formulated as crystals and encapsulated in both 0.5 and 1.5 mm SLG20 alginate capsules for IP and

Fig. 3 | In vitro release and in vivo anti-fibrotic efficacy. Agents tested in alginate spheres both in vitro and in C57BL/6 mice. **a**, In vitro GW2580 release under accelerated conditions (37 °C, PBS + 0.1% SDS) encapsulated within 2,000 μm alginate capsules. Release from crystalline formulations tuned by varying crystal size and amorphous-to-crystalline ratio (as specified). Data are mean ± s.d. **b**, Surface erosion of GW2580 large crystal over one to four weeks; original dimensions shown with pink lines. Scale bars, 100 μm. **c**, Phase-contrast and confocal images for retrieved capsules after one, three and six month IP implantations. Phase-contrast images show host FBR, observed as yellowish-white plaque on otherwise translucent alginate microspheres. Crystalline formulations encapsulated in 500 μm alginate spheres showed significant long-term anti-fibrotic efficacy. Note: drug crystals have a coloured appearance, making capsules more opaque (Supplementary Fig. 10c). Confocal images show reduced or no fibrotic overgrowth with drug crystals. Blue, DAPI nuclear stain; green, macrophage CD68; red, fibrosis marker α-SMact). Scale bars, 500 μm (phase contrast) and 50 μm (confocal). **d**, FACS analysis performed on cells dissociated from retrieved spheres after one, three and six months post-IP implantation. **e**, Images of retrieved capsules containing crystalline curcumin after six months post-IP implantation. **f**, H&E- and Masson's trichrome-stained histologic sections of three month SC implants (+tissue) showing reduced fibrosis with crystalline drugs, versus blank controls. Scale bars, 1,000 μm; ×4). **g**, Flow analysis for macrophages dissociated from spheres, (100 μl material in all cases) three months following SC implantation. **h**, Plasma drug concentrations from separate crystalline-drug formulations SC or IP implantations. Though shown to 14 d, all drugs were monitored and remained below detection limits up to 180 d. **i**, HPLC-determined capsule drug content after one, three and six months (SC and IP) for crystalline curcumin and Ki20227. **j**, LCMS determination of GW2580 levels in plasma (left y axis) versus in capsules (right y axis) following SC or IP implantation. In vitro, N=3 samples per group. All line and bar graph data are mean ± s.e.m. Statistical analysis: one-way ANOVA plus Bonferroni multiple comparison correction; **P < 0.001; ***P < 0.0001. In vivo studies, N=5 mice per group. All subpanels reflect representative data from in vitro or in vivo experimental analyses repeated three times in each case.

SC implantation in healthy NHPs as previously reported[12]. Implants were then retrieved at two and four weeks and three and/or six months (Fig. 4, Supplementary Figs. 12 and 13, and Supplementary Videos 2 and 3). The 0.5-mm-sized drug-loaded capsules remained fibrosis free and largely unattached in the IP space up to one month and in the SC site up to six months post-implant, while the 1.5-mm-sized drug-loaded capsules remained clean in both implant sites

for six months (Fig. 4 and Supplementary Fig. 12). Fibrosis-free capsules were freely dissociated from either IP omentum following peritoneal lavage during minimally invasive laparoscopic retrieval or SC tissue by biopsy punch[12]. Using phase-contrast, bright-field and laparoscopic imaging, retrieved 0.5 mm (up to one month) and 1.5 mm (up to six months) capsules appeared translucent with visible, remaining encapsulated crystalline drug and free of
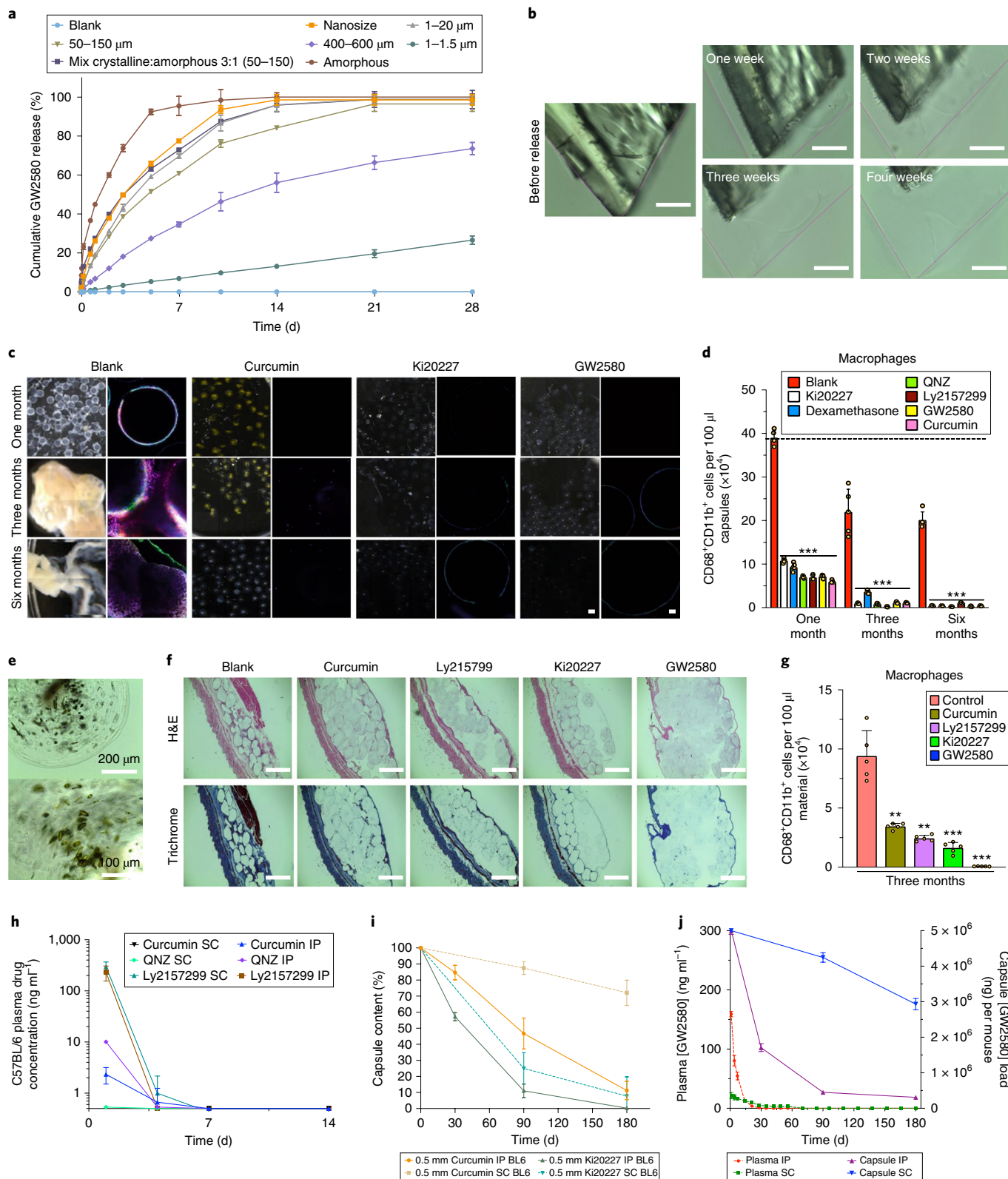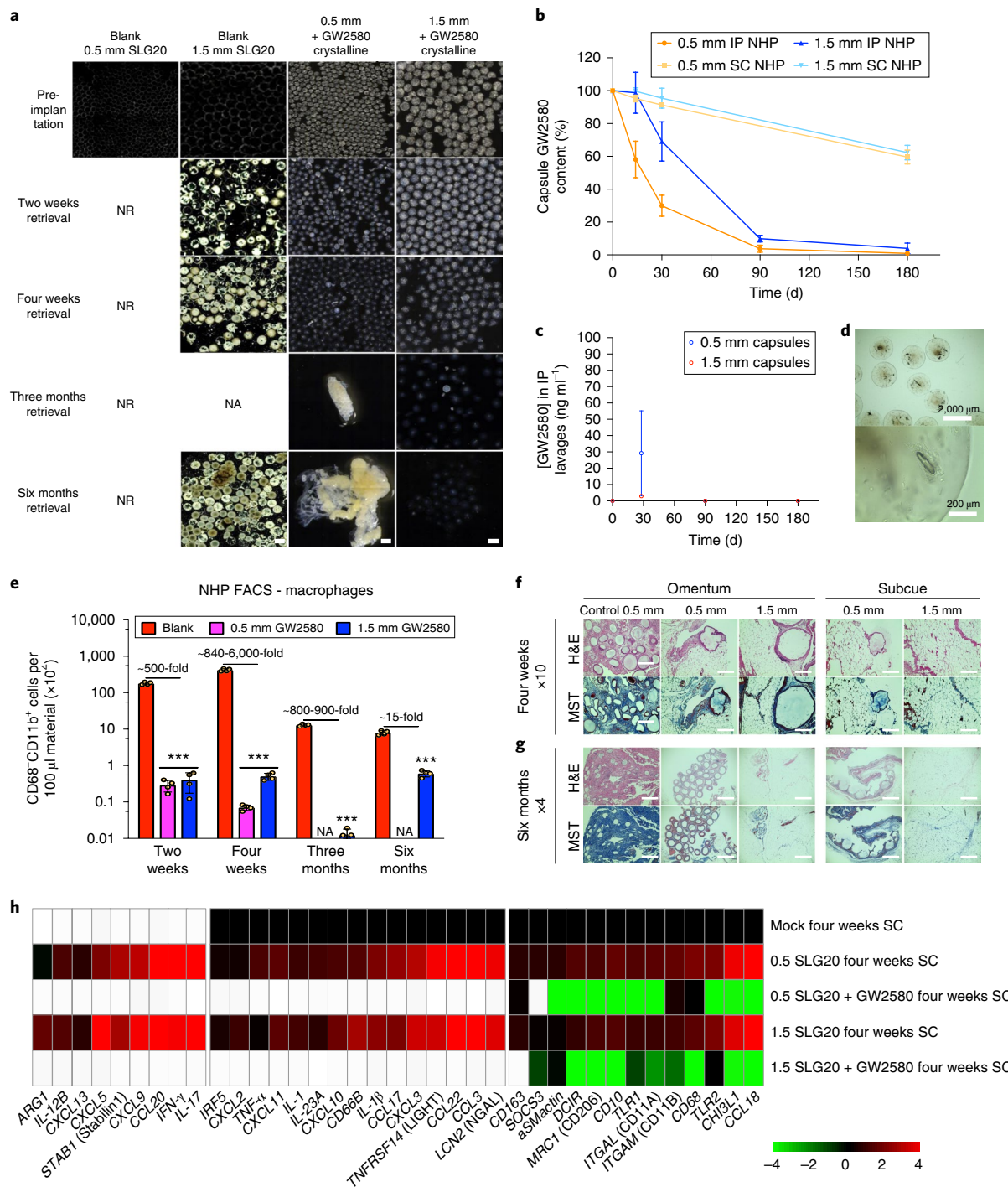
Fig. 4 | Long-term anti-fibrotic efficacy in NHPs. Crystalline GW2580 was tested in alginate spheres across different implant sites. **a**, Phase-contrast images showing host FBR against 0.5-mm- and 1.5-mm-diameter alginate spheres encapsulating crystalline CSF1R inhibitor GW2580, after two and four weeks as well as three and six months post-IP implantations in NHP; $N = 2$ per group. See Supplementary Fig. 12 for a full IP and SC implant panel over time. Note: drug crystals have coloured appearance, making drug-loaded alginate capsules more opaque/white. NR, not retrievable; NA, not available. Scale bars, 1,500 μm. **b**, Drug extraction analysis (HPLC) revealed significant crystals quantities left inside retrieved capsules (up to 8% or 68% of initial loading for IP or SC capsules, respectively). **c**, Lavage GW2580 concentrations from the IP space surrounding 0.5 mm and 1.5 mm implanted capsules. **d**, Microscopy images showing retrieved 1.5 mm capsules after six months from IP space. Crystals were found to release in a gradual manner leaving hollow spaces. **e**, Quantitative FACS analysis of cells dissociated from alginate spheres, retrieved after various post-IP implantation times, as specified, versus 1.5 mm blank SLG20 capsules. Macrophage presence is reduced with drug compared with empty (control) spheres (log base 10 scale). **f**,**g**, H&E- and Masson's trichrome (MST)-stained histological sections of excised IP omentum or SC tissue four weeks (**f**) and six months (**g**) post-implant showing reduced fibrosis in various crystalline drug (GW2580) groups, versus blank 0.5 mm control spheres. Scale bars, 400 μm (×10) or 1,000 μm (×4), respectively. **h**, NanoString analysis of four week implanted SC tissues for immune markers and cytokines, compared with mock (saline-injected) controls. White, within two s.d. of assay's mean background. All bar or line graph data are mean ± s.e.m. Statistical analysis: one-way ANOVA plus Bonferroni multiple comparison correction; ***$P < 0.0001$. $N = 4$ samples per group. All subpanels reflect representative data from in vivo experimental analyses repeated twice.

cellular overgrowth (Fig. 4a,d and Supplementary Fig. 12a–d). Correlating with the extent of FBR, remaining drug was extracted from retrieved capsules and quantified by HPLC, showing additional stores in 1.5 mm capsules in both the IP and SC sites up to six months, while 0.5 mm capsules only had remaining drug in the SC site at six months but little to no drug by three months in the IP space (Fig. 4b), suggesting faster release in the more aqueous IP compartment. Drug concentration in IP lavages was also measured at each capsule retrieval timepoint by LCMS, and was found to drop from 2–3 ng ml⁻¹ to below detection limits (0.5 ng ml⁻¹) following four weeks post-implantation for 1.5 mm capsules (Fig. 4c). Plasma analysis at the end of the study showed GW2580 levels below detection limits. Cells present on retrieved capsules were dissociated, stained and analysed by FACS. Capsules with GW2580 showed significant reduction of macrophage responses when drug was remaining (Fig. 4e).

Cryogenic SEM analysis for the capsules pre- and post-transplantation (Supplementary Fig. 13) revealed no topographic changes on the capsule surface, and show crystals shrinking with time into the surrounding cross-linked alginate matrix. As expected from previous studies in NHPs[12], 0.5 mm blank capsules implanted IP were irretrievable due to attachment to the peritoneal wall (Supplementary Fig. S9 in ref. [12]), thus limiting external comparison with 0.5 mm drug-loaded capsules. To analyse capsules without drug, we performed histology on omental tissues containing fibrosed and embedded capsules that were excised from the site of implantation at the same timepoints. Excised tissues obtained from the implant sites of drug-loaded 0.5 and 1.5 mm alginate capsules were examined through histological staining analysis (Masson's trichrome and H&E), which confirmed the lack of sphere embedding and collagen deposition over the same timeframes (Fig. 4f,g and Supplementary Fig. 12e,f). Moreover, while 0.5 mm drug-loaded capsules became clumped at three months due to low remaining drug stores, they were not extensively embedded into surrounding omental tissue until six months (Fig. 4a,e–g and Supplementary Fig. 12b,e,f).

Lastly, NanoString multiplexed gene expression analysis was performed to profile host-mediated innate immune recognition of SC drug-loaded capsules versus that of blank capsules retrieved four weeks post-implantation (Fig. 4h). Similar to C57BL/6 mouse model responses (Fig. 1b)[10,33,46], significant reduction of inflammatory macrophage markers Sphk1, TNF-α, Arg1 and IL-1, among others, was observed. We believe that further increases in crystal sizes would result in even longer release times.

Crystalline GW2580 with β-cells in diabetic mice

We next investigated whether observed improvements in biocompatibility through crystalline drug encapsulation could yield improved/prolonged function of an implanted biomedical device with living cells (Supplementary Fig. 14). Lead drugs from Fig. 1 were screened for lack of toxicity in vitro against both immortalized murine macrophage RAW264.7 cells shown by CellTiter-Glo (Supplementary Fig. 15) and against encapsulated rat islets to study the potential for impact on islet biology and function (Supplementary Fig. 16 and Supplementary Discussion 3). We evaluated rat islet function within 0.5 mm microcapsules without drug, compared with islets within 0.5 mm capsules with co-encapsulated lead candidate crystalline GW2580, after transplantation into STZ-induced diabetic C57BL/6 mice. Previously, it has been shown that 0.5-mm-sized SLG20 alginate capsules result in encapsulated islet graft cell death and loss of normoglycemia in the same model[44,52]. First, we determined that GW2580 in two forms—amorphous and crystalline—is non-toxic to co-encapsulated rat islets, at all drug loads tested (Fig. 5a and Supplementary Fig. 17a). Both drug formulations were capable of preventing loss of glucose correction for extended periods of time following transplantation into

the IP space of diabetic mice (Fig. 5b). Controls (Fig. 5b, red trend) failed, on average, by ~35 d, while amorphous (Fig. 5b, blue trend) and crystalline (Fig. 5b, green trend) formulation-loaded capsules maintained normoglycemia for either over 70 d or, much more significantly, at least 15 months or 460 d, at which time mice were terminated to analyse capsules. Macrophage depletion by clodrosome in combination with islets encapsulated in 0.5 mm SLG20 alginate islets but without drug prevented fibrosis and allowed for islet function, but induced significant toxicity by ~50–60 d post-transplantation (Fig. 5b, purple trend).

Explanted amorphous and crystalline drug-containing capsules were imaged (Fig. 5c) and analysed for rat islet function/viability marker Pdx1 and host α-SMact expression at ~430 or 460 d (~1.3 yr) post-transplant, respectively, for amorphous and crystalline GW2580 groups (Fig. 5d). Crystal GW2580 capsules had significantly higher islet viability, as indicated by ~30-fold higher Pdx1 expression, and lower myofibroblast and fibrosis response, as indicated by 74% lower α-SMact expression. The difference in Pdx1 was greater than that previously observed with larger 1.5-mm-diameter capsule size alone[12], and cures were also elongated from approximately six months with 1.5 mm capsules to over fifteen months with 0.5 mm drug-loaded capsules. Remaining crystalline formulated drug was also observed by microscopy within explanted capsules at 460 d (Fig. 5c). Lastly, by drug extraction and HPLC quantification, we found up to 27.3% of the crystalline GW2580 dose remaining in islet-containing capsules after 460 d, indicating the potential of longer-term function.

Crystalline GW2580 with human islet-transplanted SC and IP

To our knowledge, islet transplantation into an unmodified SC site (more accessible for transplantation and subsequent manipulations or replacement) has never reversed diabetes in fully immune-competent animals or humans[53]. It has been hypothesized that this environment is inhospitable to cell survival due to inadequate vascularization and poor oxygen tension[54]. Strategies for SC transplantation-based biomaterials also face the additional challenge of the fibrotic response to the encapsulating material. Physical interactions with host blood, lymph, exudate or other fluids can lead to adsorption of proteins onto the implant, including albumin, complement, fibrinogen, γ-globulin and fibronectin and eventual inflammatory response[53].

Human islets were encapsulated in 0.5 mm microcapsules, with and without crystalline GW2580, and transplanted into the IP space or injected subcutaneously in STZ-induced diabetic C57BL/6 mice. For SC delivery, the capsules were placed in two separate and elongated locations, one on each side of the animal (Supplementary Fig. 18). We hypothesized that distributing the encapsulated cells to multiple locations could reduce the oxygen and nutrient demands at each site. GW2580 in crystalline form was found to be non-toxic to co-encapsulated human islets at the same drug load of 10 mg drug per ml alginate (Supplementary Fig. 17b). Compared with control (no drug) capsules, drug-loaded capsules in both IP and SC sites were equally capable of restoring glycemic control in diabetic mice for extended periods of time up to 72 d (Fig. 5e, gold and teal trends), at which point in time the experiment was terminated to analyse samples. In contrast, SC capsules without drug did not provide control of blood sugar (Fig. 5e, red trend). These same capsules in the IP space failed after approximately 32 d, presumably due to the fibrotic response (Fig. 5e, green trend). Capsules without drug placed in the SC space were fully fibrosed, surrounded by a solid collagen sack (Fig. 5f).

Fibrosis prevention with crystalline GW2580 in PDMS discs

To examine whether crystalline-formulated drug could reduce the fibrotic response to other materials, we mixed crystalline GW2580
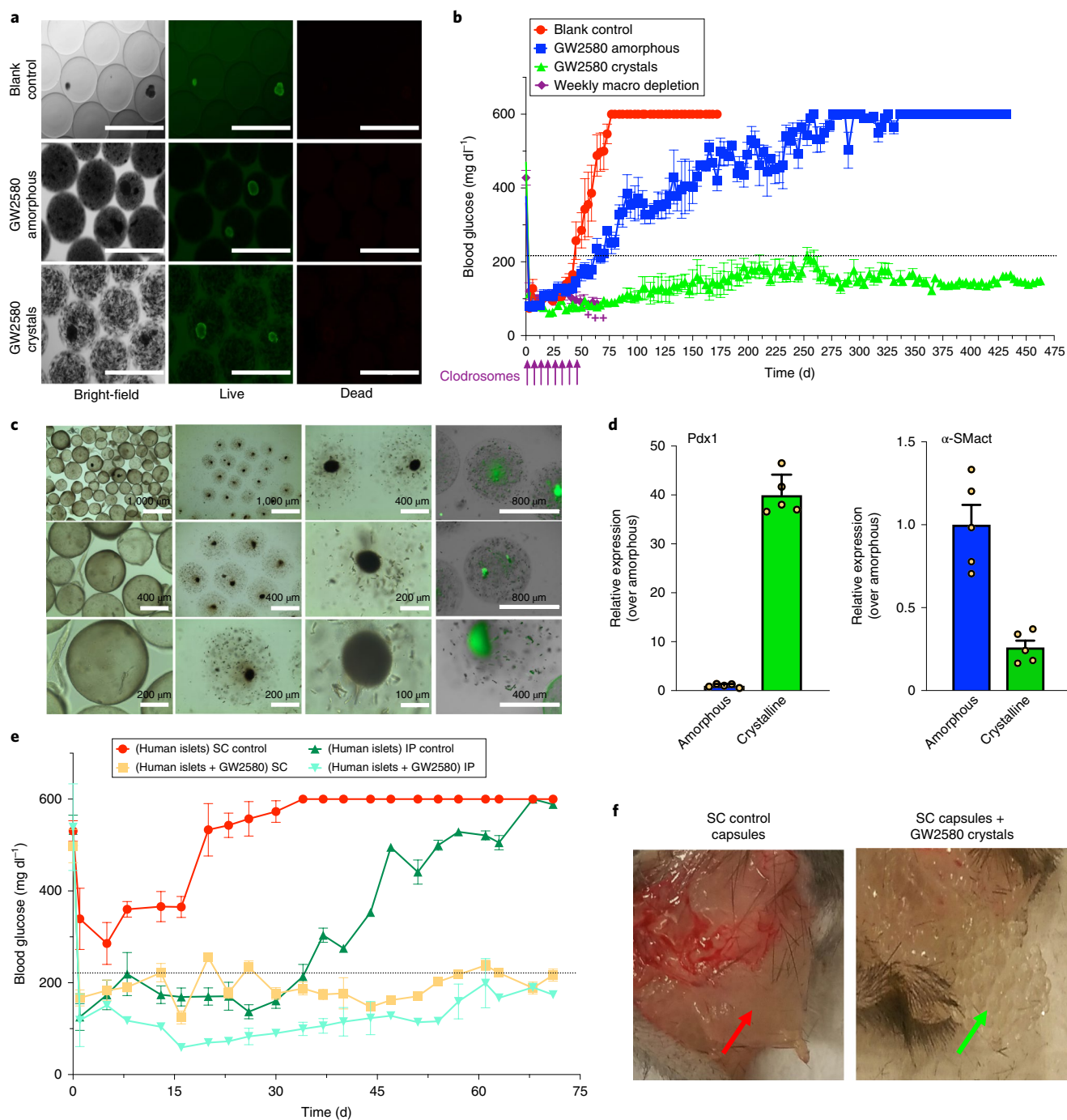
Fig. 5 | Long-term glycemic control with crystalline GW2580. Drug was co-encapsulated with islets (rat or human) and transplanted into STZ-C57BL/6 diabetic mice. **a**, Live/dead staining confirming viability of rat islet cells with both amorphous and crystalline GW2580 prepared in ~500–600 µm alginate capsules. Scale bars, 1,000 µm. Image rows: same field of view, focus and magnification. **b**, Blood glucose curves showing significantly prolonged normoglycemic maintenance with crystalline GW2580 (green), over blank (no drug, red) controls and amorphous-loaded (blue) capsules co-encapsulating 500 islet equivalents rat islets and transplanted IP. Macrophage-depleting clodrosomes (liposomal clodronate) were administered weekly (purple arrows) as positive control (++, group was terminated due to toxicity). **c**, Bright-field images of capsules after 15 months: amorphous (first column) and crystal loaded (second and third columns). Islets are visible as dark-black circles. In the fourth column, both cells and crystals under green (auto)fluorescence. **d**, Rat Pdx1 and host α-SMact expression from capsules retrieved at ~430 or 460 d (~1.3 yr) post-transplant, respectively, for amorphous and crystalline GW2580. **e**, Blood glucose curves showing prolonged normoglycemia for ~500–600 µm capsules co-encapsulating 2,000 islet equivalents human islets transplanted in diabetic C57BL/6 mice with GW2580 crystals (gold, SC; teal-blue, IP) versus without (red, SC; green, IP). Capsules without GW2580 failed after ~32 d in the IP space, and in the SC space did not provide glycemic control. In contrast, capsules with GW2580 crystals provided glycemic control for over 72 d (termination timepoint) in both IP and SC. **f**, Photos showing control and GW2580-loaded capsules retrieved after the 72 d SC transplantation. Control capsules were fully fibrosed forming a solid collagen-encapsulated sack, compared with fibrosis-free crystalline GW2580-loaded capsules. All line/bar graph data are mean ± s.e.m. Statistical analysis: one-way ANOVA plus Bonferroni multiple comparison correction; **$P < 0.001$; ***$P < 0.0001$. In vivo studies, $N = 5$ mice per group. All subpanels reflect representative data from experimental analyses repeated twice.
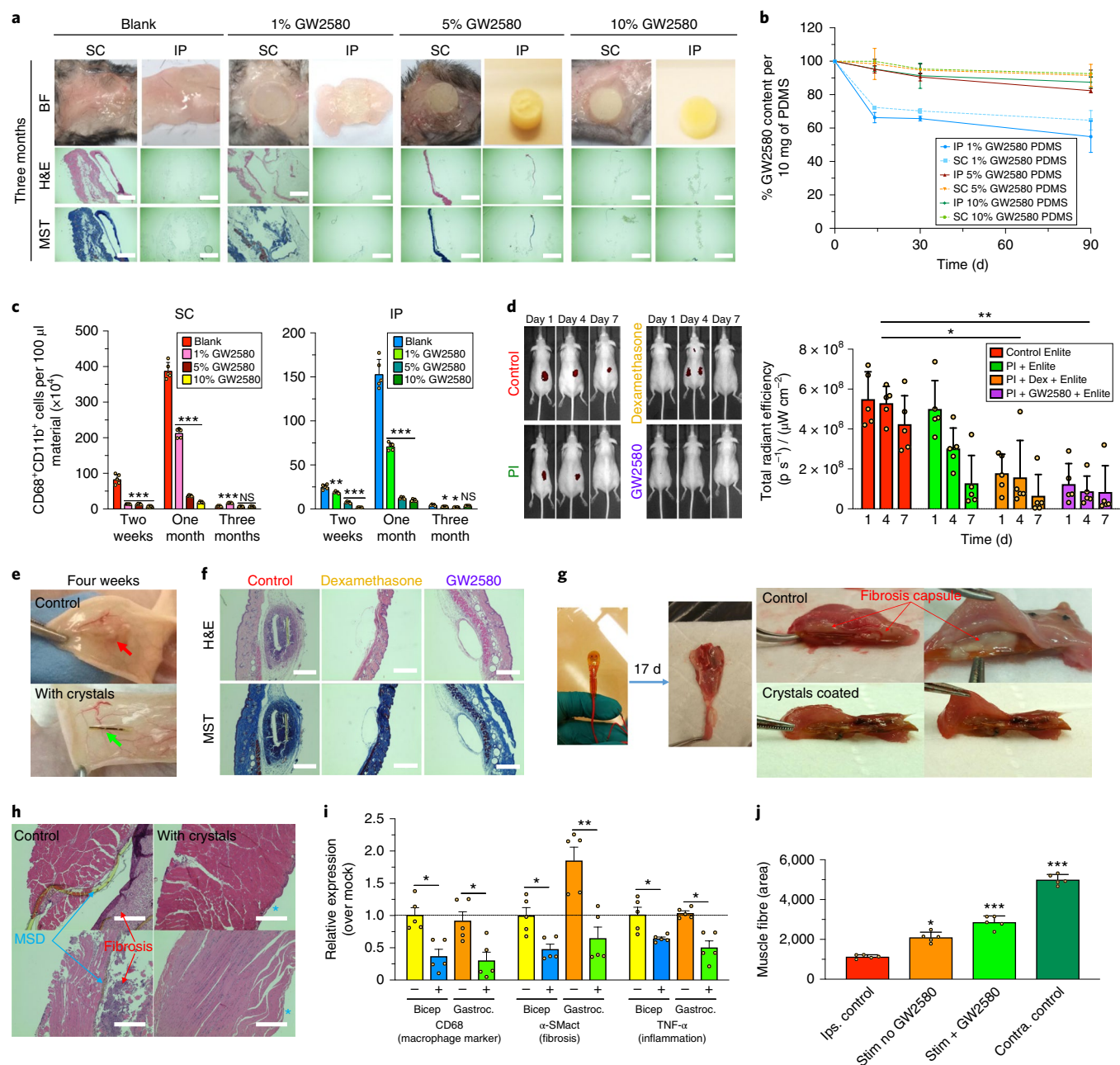
Fig. 6 | Long-term drug depot effects of GW2580 crystals. Drug was loaded within cured PDMS discs or surface coatings on multicomponent devices. **a**, Bright-field (BF), H&E and Masson's trichrome histology images of excised three month SC and IP tissue + PDMS discs, loaded with 0 (blank), 1, 5 or 10% crystalline GW2580, in C57BL/6 mice. Scale bars, 1,000 μm; ×4 (Supplementary Fig. 19). **b**, GW2580 loading % (by HPLC) following SC or IP three month implantation. **c**, Flow analysis for macrophages dissociated from discs three months SC and IP post-implantation. **d**, IVIS-measured implant-induced SC inflammation using ProSense at 1, 4 and 7 d post-insertion in SKH1 mice. Native CGMs (control), polyimide (PI)-coating alone or with crystalline drug (dexamethasone (Dex) or GW2580) were used. **e**, Photos showing crystalline GW2580-coated CGMs with reduced fibrosis after four weeks SC implantations, versus controls. **f**, H&E and Masson's trichrome staining of excised four week SC implants, showing reduced fibrosis with crystalline drug (either dexamethasone or GW2580), compared with control CGMs. Scale bar, 400 μm (×10). **g**, Retrieved MSDs 17 d after suturing to gastrocnemius muscle (IM implantation) in rats. Cross-section images: thick fibrosis for controls (>500 μm) versus no significant fibrosis with crystalline GW2580. **h**, H&E-stained sections of tissues excised 17 d post-IM implant, confirming dramatic to complete fibrosis reduction along with larger muscle fibre density with crystalline GW2580. In contrast, controls had thick fibrosis and significant muscle atrophy, following daily muscle stimulation over two weeks. Blue asterisks denote location of implants that were not retained following sectioning due to lack of fibrosis. Scale bars, 400 μm. **i**, Gene expression analysis performed on bicep and gastrocnemius (Gastroc.) muscles retrieved post-stimulation indicates reduced macrophage marker CD68, fibrosis marker α-SMact and inflammatory TNF-α for crystalline GW2580-coated MSDs. **j**, Quantitative analysis of muscle atrophy. All line and bar graph data are mean ± s.e.m. Statistical analysis: one-way ANOVA plus Bonferroni multiple comparison correction *P < 0.05; **P < 0.001; ***P < 0.0001; NS, not significantly different. In vivo, N = 5 animals per group. Ips., ipsalateral; Stim., stimulation; Contra., contralateral. All subpanels reflect representative data from experimental analyses repeated twice for MSDs or three times for PDMS and CGMs.

into polydimethylsiloxane (PDMS) at 0, 1, 5 or 10% w/w before to curing into discs (Fig. 6a and Supplementary Fig. 19a). This was done to first establish anti-fibrotic efficacy within a known single biomaterial, PDMS, which is Food and Drug Administration approved for numerous device systems including breast implants and cannulas, for which SC and IP sites are more relevant for biocompatibility and drug-release assessment. Discs with and without GW2580 were then implanted both IP and SC for two and four weeks and three months in C57BL/6 mice (one disc per site per mouse). FBR, observed as yellowish-pink tissue on retrieved PDMS discs, was reduced in a dose-dependent fashion by all drug concentrations at two and four weeks as well as three months (Fig. 6a and Supplementary Fig. 19b–c). Masson's trichrome and H&E histological staining of both excised SC and IP samples confirmed significantly reduced immune cell infiltration and fibrosis, compared with blank (no drug) control discs (Fig. 6a and Supplementary Fig. 19c). Determination of remaining drug levels by HPLC, following either SC or IP implantation for all timepoint incubations, once again confirmed that release was slower in the SC space (Fig. 6b). Flow analysis for responding macrophages dissociated from retrieved discs showed significant reductions in cell numbers between drug-containing discs and no drug controls at all timepoints for IP implantations, and at two weeks and one month for SC implantations (Fig. 6c). While macrophage levels remained low for all drug-containing discs at three months, levels detected on control (no drug) discs significantly decreased over time, resulting in a lack of relative difference at three months in the SC space. We have observed this phenomenon of decreasing immunologic engagement over time for other untreated material implants at late (>2–3 month) timepoints (Figs. 3d and 4e). As fibrotic encapsulation becomes more complete, macrophage density around the implants decreases. Drug retention was also much higher in PDMS compared with alginate hydrogel capsules, over the same incubation times, mainly due to limited swelling ability (Fig. 6b versus Fig. 3j).

Crystalline GW2580 along with multicomponent devices

The utility of crystalline GW2580 was also evaluated with multicomponent devices composed of different materials, including plastic composites, metal alloys and enzymes. Two different implant models were tested: (1) device sensors for collecting information from the host and (2) devices that exert a function on the surrounding host tissues. We chose CGM Enlite sensors (second generation) and an in-house-manufactured MSD (Supplementary Fig. 20a and Fig. 6d–f, and Supplementary Fig. 20b and Fig. 6g–j, respectively). Drug crystals were add to fast thermo-curing polyimide[55] and applied as top coatings onto the implantable part of each device (Supplementary Fig. 21 and Supplementary Discussion 4). Coated CGM sensors were studied in their clinically relevant site of use (SC) in hairless SKH1 mice, which show intact subcutaneous inflammation and fibrotic responses similar to C57BL/6 mice[11] while not requiring additional shaving and use of Nair to remove signal detection interference[10], with in vivo imaging system (IVIS) whole body imaging for implant-induced inflammation at 1, 4 and 7 d post-insertion. The incorporated crystals significantly reduced implant-induced inflammation (Fig. 6d). After four weeks, sensors were retrieved and analysed. As opposed to no drug controls, crystalline GW2580 drug-coated CGMs had little to no fibrotic encapsulation, as determined by histological staining (Fig. 6e,f). Crystalline GW2580 efficacy in a second multicomponent MSD model was also evaluated at a different implantation site, that is, intramuscular (IM). In our model the inflammation/immune and fibrosis responses persist, specifically in the gastrocnemius and bicep muscles, which are the immediately adjacent tissues. As such, MSDs were sutured to gastrocnemius muscle of Sprague–Dawley rats, relevant for muscle atrophy studies, following severing of the tibial nerve, and daily muscle stimulation was performed for 2 weeks starting

at 3 d post-implantation. Devices were retrieved at 17 d. Control MSDs without drug were associated with thick fibrosis for controls (>500 μm), while GW2580-coated MSDs had no significant fibrosis (Fig. 6g). This was confirmed by H&E-stained histological sections of surrounding muscle tissues, showing substantial reduction of fibrosis along with a larger density of muscle fibres with drug-loaded MSDs (Fig. 6h). Quantitative gene expression analysis on the device and surrounding muscle indicated reductions of macrophage marker CD68, fibrosis marker α-SMac and inflammatory TNF-α for crystalline drug-coated MSDs (Fig. 6i). Device function enhancement was also confirmed by quantitative analysis of muscle atrophy (Fig. 6j). Less muscle atrophy was found when drug-loaded MSDs were used, likely due to prevention of the fibrotic capsule and improved stimulation and enervation of the surrounding tissue.

In summary, we have developed crystalline, anti-inflammatory drug formulations that are capable of providing local, long-term, non-toxic control of fibrosis. Release kinetics of these drugs could be tuned by controlling several parameters, including crystalline degree, compositions, crystal form, crystal size and morphology. The compact nature of these crystals is supported by hydrophobic chemical moiety interactions and inter- and intramolecular hydrogen bonds, limiting the rate of infiltration by water resulting in slow release through surface erosion/dissolution. We demonstrate the potential of this approach with a number of anti-inflammatory drugs, and identify formulations that can be utilized for slow release over months to years.

One crystal formulation of particular interest is GW2580, a CSF1R small inhibitor, which we demonstrate has the potential to provide local control of fibrosis in a range of settings. When encapsulated in alginate microspheres, crystalline GW2580 could suppress fibrosis in both rodents and non-human primates (Figs. 3 and 4). When islets were included in these formulations, these capsules were able to provide long-term control of blood sugar in diabetic C57BL/6 mice, with both human and rat islets (Fig. 5). Interestingly, these formulations allowed for significant, albeit imperfect, control of blood sugar following placement in the subcutaneous space. We have demonstrated a formulation capable of providing blood sugar control with human cells in C57BL/6 mice subcutaneously. Finally, we have demonstrated that crystalline GW2580 is able to significantly reduce the fibrosis and improve performance on two different multicomponent devices, a CGM and an electrical MSD (Fig. 6). We believe the formulations described here could have utility in a range of device applications including cellular transplantation, implantable stimulators and sensors, and prosthesis for tissue engineering.

Online content

Any methods, additional references, Nature Research reporting summaries, source data, statements of code and data availability and associated accession codes are available at https://doi.org/10.1038/s41563-019-0377-5.

References

1. Fattahi, P., Yang, G., Kim, G. & Abidian, M. R. A review of organic and inorganic biomaterials for neural interfaces. *Adv. Mater.* **26**, 1846–1885 (2014).
2. Nichols, S. P., Koh, A., Storm, W. L., Shin, J. H. & Schoenfisch, M. H. Biocompatible materials for continuous glucose monitoring devices. *Chem. Rev.* **113**, 2528–2549 (2013).
3. Rosen, M. R., Robinson, R. B., Brink, P. R. & Cohen, I. S. The road to biological pacing. *Nat. Rev. Cardiol.* **8**, 656–666 (2011).
4. Farra, R. et al. First-in-human testing of a wirelessly controlled drug delivery microchip. *Sci. Transl. Med.* **4**, 122ra121 (2012).
5. Hubbell, J. A. & Langer, R. Translating materials design to the clinic. *Nat. Mater.* **12**, 963–966 (2013).
6. Kearney, C. J. & Mooney, D. J. Macroscale delivery systems for molecular and cellular payloads. *Nat. Mater.* **12**, 1004–1017 (2013).

7. Yoo, J. W., Irvine, D. J., Discher, D. E. & Mitragotri, S. Bio-inspired, bioengineered and biomimetic drug delivery carriers. *Nat. Rev. Drug Discov.* **10**, 521–535 (2011).

8. Kenneth Ward, W. A review of the foreign-body response to subcutaneously-implanted devices: the role of macrophages and cytokines in biofouling and fibrosis. *J. Diabetes Sci. Technol.* **2**, 768–777 (2008).

9. Anderson, J. M., Rodriguez, A. & Chang, D. T. Foreign body reaction to biomaterials. *Semin. Immunol.* **20**, 86–100 (2008).

10. Doloff, J. C. et al. Colony stimulating factor-1 receptor is a central component of the foreign body response to biomaterial implants in rodents and non-human primates. *Nat. Mater.* **16**, 671–680 (2017).

11. Vegas, A. J. et al. Combinatorial hydrogel library enables identification of materials that mitigate the foreign body response in primates. *Nat. Biotechnol.* **34**, 345–352 (2016).

12. Veiseh, O. et al. Size- and shape-dependent foreign body immune response to materials implanted in rodents and non-human primates. *Nat. Mater.* **14**, 643–651 (2015).

13. Rhen, T. & Cidlowski, J. A. Antiinflammatory action of glucocorticoids—new mechanisms for old drugs. *N. Engl. J. Med.* **353**, 1711–1723 (2005).

14. Schneider, B. L., Schwenter, F., Pralong, W. F. & Aebischer, P. Prevention of the initial host immuno-inflammatory response determines the long-term survival of encapsulated myoblasts genetically engineered for erythropoietin delivery. *Mol. Ther.* **7**, 506–514 (2003).

15. Zhang, W. J. et al. HOE 077 reduces fibrotic overgrowth around the barium alginate microcapsules. *Transplant. Proc.* **32**, 206–209 (2000).

16. Attur, M. G. et al. Differential anti-inflammatory effects of immunosuppressive drugs: cyclosporin, rapamycin and FK-506 on inducible nitric oxide synthase, nitric oxide, cyclooxygenase-2 and PGE 2 production. *Inflamm. Res.* **49**, 20–26 (2000).

17. Cannarile, M. A. et al. Colony-stimulating factor 1 receptor (CSF1R) inhibitors in cancer therapy. *J. Immunother. Cancer* **5**, 53 (2017).

18. Wehling, M. Non-steroidal anti-inflammatory drug use in chronic pain conditions with special emphasis on the elderly and patients with relevant comorbidities: management and mitigation of risks and adverse effects. *Eur. J. Clin. Pharmacol.* **70**, 1159–1172 (2014).

19. Srinivasan, A. & De Cruz, P. Review article: a practical approach to the clinical management of NSAID enteropathy. *Scand. J. Gastroenterol.* **52**, 941–947 (2017).

20. Lin, J. et al. TNFα blockade in human diseases: an overview of efficacy and safety. *Clin. Immunol.* **126**, 13–30 (2008).

21. Gyorfi, A. H., Matei, A. E. & Distler, J. H. W. Targeting TGF-β signaling for the treatment of fibrosis. *Matrix Biol.* **68–69**, 8–27 (2018).

22. Murray, P. J. & Wynn, T. A. Protective and pathogenic functions of macrophage subsets. *Nat. Rev. Immunol.* **11**, 723–737 (2011).

23. Dang, T. T. et al. Spatiotemporal effects of a controlled-release anti-inflammatory drug on the cellular dynamics of host response. *Biomaterials* **32**, 4464–4470 (2011).

24. Singarayar, S., Kistler, P. M., De Winter, C. & Mond, H. A comparative study of the action of dexamethasone sodium phosphate and dexamethasone acetate in steroid-eluting pacemaker leads. *Pacing Clin. Electrophysiol.* **28**, 311–315 (2005).

25. Friedl, K. E. Corticosteroid modulation of tissue responses to implanted sensors. *Diabetes Technol. Ther.* **6**, 898–901 (2004).

26. Gilligan, B. C. et al. Feasibility of continuous long-term glucose monitoring from a subcutaneous glucose sensor in humans. *Diabetes Technol. Ther.* **6**, 378–386 (2004).

27. Vacanti, N. M. et al. Localized delivery of dexamethasone from electrospun fibers reduces the foreign body response. *Biomacromolecules* **13**, 3031–3038 (2012).

28. Weldon, C. B. et al. Electrospun drug-eluting sutures for local anesthesia. *J. Control. Release* **161**, 903–909 (2012).

29. Ricci, M. et al. Ketoprofen controlled release from composite microcapsules for cell encapsulation: effect on post-transplant acute inflammation. *J. Control. Release* **107**, 395–407 (2005).

30. Einmahl, S. et al. Concomitant and controlled release of dexamethasone and 5-fluorouracil from poly (ortho ester). *Int. J. Pharm.* **185**, 189–198 (1999).

31. Siepmann, J., Siegel, R. A. & Rathbone, M. J. (eds) *Advances in Delivery Science and Technology* (Springer, 2012).

32. Bain, C. C. et al. Constant replenishment from circulating monocytes maintains the macrophage pool in the intestine of adult mice. *Nat. Immunol.* **15**, 929–937 (2014).

33. Mosser, D. M. & Edwards, J. P. Exploring the full spectrum of macrophage activation. *Nat. Rev. Immunol.* **8**, 958–969 (2008).

34. Singh, M. N., Hemant, K. S., Ram, M. & Shivakumar, H. G. Microencapsulation: a promising technique for controlled drug delivery. *Res. Pharm. Sci.* **5**, 65–77 (2010).

35. Cobelli, N., Scharf, B., Crisi, G. M., Hardin, J. & Santambrogio, L. Mediators of the inflammatory response to joint replacement devices. *Nat. Rev. Rheumatol.* **7**, 600–608 (2011).

36. Desbois, S., Seabrook, S. A. & Newman, J. Some practical guidelines for UV imaging in the protein crystallization laboratory. *Acta Crystallogr. F* **69**, 201–208 (2013).

37. Niedzialkowska, E. et al. Protein purification and crystallization artifacts: the tale usually not told. *Protein Sci.* **25**, 720–733 (2016).

38. Farah, S., Khan, W. & Domb, A. J. Crystalline coating of rapamycin onto a stent: process development and characterization. *Int. J. Pharm.* **445**, 20–28 (2013).

39. Levy, Y., Khan, W., Farah, S. & Domb, A. J. Surface crystallization of rapamycin on stents using a temperature induced process. *Langmuir* **28**, 6207–6210 (2012).

40. Puhl, S., Meinel, L. & Germershaus, O. Recent advances in crystalline and amorphous particulate protein formulations for controlled delivery. *Asian J. Pharm. Sci.* **11**, 469–477 (2016).

41. Yaghmur, A., Rappolt, M., Ostergaard, J., Larsen, C. & Larsen, S. W. Characterization of bupivacaine-loaded formulations based on liquid crystalline phases and microemulsions: the effect of lipid composition. *Langmuir* **28**, 2881–2889 (2012).

42. Farah, S. Protective layer development for enhancing stability and drug-delivery capabilities of DES surface-crystallized coatings. *ACS Appl. Mater. Interfaces* **10**, 9010–9022 (2018).

43. Kalepu, S. & Nekkanti, V. Insoluble drug delivery strategies: review of recent advances and business prospects. *Acta Pharm. Sin. B* **5**, 442–453 (2015).

44. Dang, T. T. et al. Enhanced function of immuno-isolated islets in diabetes therapy by co-encapsulation with an anti-inflammatory drug. *Biomaterials* **34**, 5792–5801 (2013).

45. Wu, P. & Grainger, D. W. Drug/device combinations for local drug therapies and infection prophylaxis. *Biomaterials* **27**, 2450–2467 (2006).

46. Murray, P. J. et al. Macrophage activation and polarization: nomenclature and experimental guidelines. *Immunity* **41**, 14–20 (2014).

47. Chadha, R., Arora, P., Saini, A. & Jain, D. S. Solvated crystalline forms of nevirapine: thermoanalytical and spectroscopic studies. *AAPS PharmSciTech* **11**, 1328–1339 (2010).

48. Chadha, R., Kuhad, A., Arora, P. & Kishor, S. Characterisation and evaluation of pharmaceutical solvates of Atorvastatin calcium by thermoanalytical and spectroscopic studies. *Chem. Cent. J.* **6**, 114 (2012).

49. Olafson, K. N., Ketchum, M. A., Rimer, J. D. & Vekilov, P. G. Mechanisms of hematin crystallization and inhibition by the antimalarial drug chloroquine. *Proc. Natl Acad. Sci. USA* **112**, 4946–4951 (2015).

50. Datta, S. & Grant, D. J. Crystal structures of drugs: advances in determination, prediction and engineering. *Nat. Rev. Drug Discov.* **3**, 42–57 (2004).

51. Kempster, C. J. E. & Lipson, H. A rapid method for assessing the number of molecules in the unit cell of an organic crystal. *Acta Crystallogr. B* **28.12**, 3674–3674 (1972).

52. de Groot, M., Schuurs, T. A. & van Schilfgaarde, R. Causes of limited survival of microencapsulated pancreatic islet grafts. *J. Surg. Res.* **121**, 141–150 (2004).

53. Pepper, A. R. et al. A prevascularized subcutaneous device-less site for islet and cellular transplantation. *Nat. Biotechnol.* **33**, 518–523 (2015).

54. Simeonovic, C. J., Dhall, D. P., Wilson, J. D. & Lafferty, K. J. A comparative study of transplant sites for endocrine tissue transplantation in the pig. *Aust. J. Exp. Biol. Med. Sci.* **64**, 37–41 (1986).

55. Georgiev, A. et al. in *High Performance Polymers—Polyimides Based: From Chemistry to Applications* (ed. Abadie, J. M.) Ch. 4 (Intech, 2012).

Acknowledgements

Author contributions

S.F., J.C.D., and D.G.A. designed the studies, analysed data and wrote the paper. S.F., J.C.D., P.M., A.S., H.J.H., K.O., K.V., H.H.T., J.H.-L., P.S.K., M.G., A.M., M.M., A.C.G., J.M. and J.O. conducted the experiments. S.F. and J.C.D. carried out the statistical analyses and prepared displays communicating data sets. G.C.W. and D.L.G. provided advice and technical support throughout. R.L. and D.G.A. supervised the study. All authors discussed the results and the preparation of the paper.

Competing interests

The authors declare no competing interests.

Additional information

Supplementary information is available for this paper at https://doi.org/10.1038/s41563-019-0377-5.

Reprints and permissions information is available at www.nature.com/reprints.

Correspondence and requests for materials should be addressed to D.G.A.

Publisher's note: Springer Nature remains neutral with regard to jurisdictional claims in published maps and institutional affiliations.

Methods

Materials. In vitro reagents were purchased from Life Technologies, unless otherwise mentioned. The antibodies (Fluor-conjugated anti-mouse Ly-6G/Ly-6C (Gr-1), CD11b and CD68) were purchased from BioLegend and used as described below. For NHP immunostaining, anti-human CD68 antibody Alexa Fluor conjugated was purchased from Santa Cruz. The CD11b (anti-mouse/human) antibody (from BioLegend) was used the same for both mouse and primate staining. The 425–600 μm acid-washed glass spheres (catalogue no./lot no. G8772/SLBL7288V) and Cy3-conjugated anti-mouse α-SMact antibody were purchased from Sigma-Aldrich. The Dow Sylgard 184 silicone elastomer-PDMS curing kit was purchased from Dow Corning. Alginate-PRONOVA SLG20 was purchased from NovaMatrix. Materials used in this study were tested for endotoxin content by a commercial vendor (Charles River) and it was found that spheres contained endotoxin levels below the detection limit (<0.05 EU ml^{-1}). Polyimide 2525 was purchased from HD Microsystems. All the solvents were analytical grade and purchased from Sigma-Aldrich. Sodium dodecyl sulfate (SDS) was purchased from Sigma-Aldrich. Drugs were purchased from various vendors: rapamycin and dexamethasone (Sigma-Aldrich), GW2580 (LC Laboratories), LY2157299 and QNZ (Cayman), curcumin (Enzo), Ki20227, A83-01 and D4476 (Tocris), CAL-101 and lenalidomide/CC-5013 (Selleck Chem), and cFMS Receptor Inhibitor III (EMD Millipore).

Preparation of crystals. In this study, three different crystallization techniques (MI–MIII) were used for crystal preparation and the resulting crystals were confirmed by microscopy methods and XRD for lattice structure, density and polymorphism.

MI: solvent evaporation-induced crystallization. Drugs were solubilized in acetone in undersaturated levels and then the solvent was allowed to evaporate at room temperature to allow crystals to form. Crystals were collected and analysed as mentioned above. A wide range of crystal sizes was obtained, along with the major portion of crystals characterized with twinning.

MII: temperature-induced crystallization. Drugs were solubilized at oversaturation in DMSO using heating (50–120 °C) followed by fast cooling to room temperature or to 4 °C. Then solutions were kept from 30 min to 24 hours to complete crystal growth. Crystals were collected and analysed as mentioned above.

MIII: crystallization in solvent/anti-solvent mixture. All crystals were grown at constant temperature (20–30 °C) using solvent/anti-solvent mixing methods with concentrations ranging from of hydrophobic compounds 0.001 to 5,000 mg ml^{-1}, where the anti-solvent was added in portions. Ethyl acetate (EA) was used as a solvent while hexane (HE) was used as an anti-solvent. For example, hydrophobic compounds, in particular, 100 mg of curcumin, 100 mg of dexamethasone, 100 mg of Ly215799 and 100 mg of GW2580, were each initially dissolved in 5 to 150 ml EA. In some crystallization experiments, solvent solutions were sonicated up to 15 min and/or pre-heated in a range from 20 to 80 °C to facilitate solubility. To the solutions of each of these hydrophobic compounds, HE was added in sub-portions to fit a range of 0 to 150 ml per 100 mg dissolved hydrophobic compound in EA, depending on the desired final crystal size range. Resulting mixtures were then incubated at stable temperature, that is, 20–30 °C. The process was optimized for minutes to hours depending on the molecular structure of the compound, and desired crystal size range; for example, 100 mg of dexamethasone was dissolved in 40 ml EA, and 30 ml of HE was added and the process was fit to 4 h, yielding crystals with a size range 40–80 μm. Controlling crystal size depends on various conditions that need to be optimized, that is, drug concentration, solvent:anti-solvent ratio, temperature, process time and so on.

Amorphous materials preparation. The amorphous form was prepared for drugs in this study by two methods depending whether cells were encapsulated with drug or not.

With no cells in encapsulation: the amorphous material was prepared inside the polymer solution (hydrogel) by first dissolving the drug in DMSO (in a minimum volume). Then the dissolved drug was added to the polymer solution to fit a desired drug concentration per ml of mixture (with the vast majority of the mixture volume, ≥70%, by volume, being aqueous). By mixing, the two solvents interfere and uniformly push the drugs quickly out of the DMSO to be trapped inside the aqueous solution/hydrogel/polymer matrix in an amorphous form, with drugs being finely dispersed inside this mixture. The amorphous % yield is ≥90% (due to self-crystallization in some cases). This suspension/mixture was further encapsulated to make capsules release drug in a burst manner (days to couple of weeks duration). Amorphous-based formulations were prepared fresh before implantation to avoid self-crystallization due to limited stability.

This method can be applied to any homogeneously able-to-be-mixed solvent system where the first solvent is the drug solvent and the second is anti-solvent (where an encapsulating polymer may be dissolved, or not, and where the anti-solvent is the major constituent in the final mixture: ≥70%). Supplementary Fig. 1a shows representative amorphous formulations prepared in situ by this method inside hydrogel alginate.

When cells are involved in the encapsulation process: to a glass vial fixed on a hot plate (40–50 °C) continuously flushed with N$_2$ or Ar, a saturated drug solution (drug + minimum volume of solvent) was added in a droplet manner. On first contact between the drug solution and hot glass surface, the solvent immediately evaporates and results with the drug in amorphous form. The fast-produced amorphous drug, in white powder form, was immediately collected and used for co-encapsulation with cells. The amorphous % yield is ≥70% (due to self-crystallization in some cases and how fast evaporation occurs depending on the solvent). Also in this case, amorphous-based formulations were prepared fresh before implantation to avoid self-crystallization due to limited stability.

SXRD and PXRD. SXRD: for all structures, intensities were recorded using a Bruker-AXS X8 Kappa diffractometer, performing φ- and ω-scans. The instrument was equipped with a Bruker APEX2 CCD and an Oxford Cryosystems CryoStream 700 Plus set to 100 K. The diffractometer was further equipped with two IμS microsources emitting Mo Kα radiation ($\lambda = 0.71073$ Å) or Cu Kα radiation ($\lambda = 1.54178$ Å). The programs SAINT[56] and SADABS[57] were employed for data reduction and scaling, respectively. The program SHELXT[58] was used to solve the phase problem and the program SHELXL[59] was used for structure refinement against F^2 on all data. Generally established refinement methods were employed[60]. All atoms (except hydrogen) were treated as anisotropic. Hydrogen atoms on carbon were placed in their calculated positions and refined using a riding model. Hydrogen atoms on nitrogen or oxygen were located in the difference density map and were refined using distance restraints with target values of 0.84(2) Å for O–H and 0.91(2) for N–H distances. The U_{iso} values of all hydrogen atoms were constrained to be 1.2 or 1.5 times the U_{eq} of the atoms to which they bind. Some structures contained disorders. Those disorders were refined using similar distance restraints for bonds and angles. In addition, similarity and rigid bond restraints were employed for the thermal parameters of disordered atoms.

PXRD: powder diffraction experiments were carried out at low temperature (100 K) with Cu Kα radiation ($\lambda = 1.54178$ Å) using a single-crystal diffractometer (Bruker-AXS X8 with APEX2 detector; the same instrument was used for the single-crystal data collections as well). The powder samples were held in a polyimide capillary that was rotating around its axis during data collection.

In situ accelerated release microscopy monitoring. GW2580 crystals form samples were placed on glass slides with glass cover slips separated by selotip. To these samples, PBS + 0.3% (w/v) SDS (to expedite the dissolution rate) was added, incubated at 37 °C and in situ monitored. For the microscopy monitoring purpose, we used the DeltaVision Elite Widefield Deconvolution System (GE Healthcare) with filters: excitation 475 nm, emission 525 nm = standard FITC/GFP filter set with objective lens: ×10, 0.4 numerical aperture Plan Fluor. Samples were monitored for 24 h at 37 °C.

Ex situ and in situ AFM. We employed time-resolved AFM as a technique to study on the molecular level the mechanism of drug release. Single crystals were prepared for ex situ and in situ observation in air and in solution to identify the dominant drug-release mechanisms as well as to determine the kinetics between crystal forms. We employed a Cypher ES Environmental atomic force microscope from Asylum Research for all experiments. The sealed liquid cells for the Cypher AFM are specifically designed with materials that are compatible for harsh solvent conditions. This atomic force microscope provides the ability to probe samples with environmental control, including precise temperature control with the modular sample stage. In this way, we were able to monitor drug release in ambient conditions (25 °C) during ex situ measurements before in situ, wherein we increased and maintained the temperature at 37 °C during solution exchange.

Attachment of crystals for AFM. AFM measurements were performed with crystal forms 1 and 2. F1 (MII) and F2 (MIII), respectively, were crystals fixed on an epoxy substrate. Single crystals were attached using a thin film of partially cured epoxy (MasterBond EP21AOLV) on Ted Pella 15 mm metal discs. The epoxy was partially cured at 60 °C for 30 min before depositing the crystals using a statically charged pipette tip. All crystals were used for in situ observation within 1 h of sample preparation.

In situ AFM image collection. AFM images were collected via Olympus TR800PSA probes (Silicon nitride-probe: (5/30) Cr/Au coated and spring constant: 0.15 N m^{-1}) with a contact mode and ca. 32 kHz as a tapping frequency. Image sizes ranged from 1 to 10 μm with scan rates between 2 and 5 Hz, and 256 scan lines per image. Height and deflection imaging modes were employed for data analysis and image selection. We processed height and deflection images by second-order flattening and image contrast adjustment. No low pass, median, or two-dimensional fast Fourier transform filters were applied to any of the AFM images.

In situ monitoring of the mechanism of drug release. We attached single crystals to AFM sample pucks using epoxy, as described above, on the same day that we conducted the experiments. The sample were placed on the AFM scanner which was initially at 25 °C. Ex situ images were collected of the (001) F1 and F2 crystal surfaces at 25 °C before introduction of solution. From these AFM images, we identified the crystal edges to determine the crystallographic directions on the upward-facing (001) crystallographic faces for both F1 and F2 crystals.

We loaded the AFM fluid cell with reagent-grade PBS and allowed it to thermally equilibrate to ambient temperature before being introduced into the AFM liquid cell. The solution was fully undersaturated on being introduced. On introducing the undersaturated PBS, the temperature was set to 37 °C and was maintained at a constant in situ temperature for the duration of the experiment. We recorded the time between introducing the solution, heating until thermal equilibration was achieved, and the AFM cantilever tip engaging with the surface, which we denoted by t_0. AFM images were continuously collected and the undersaturated solution was exchanged to maintain a constant degree of undersaturation. Different regions of each crystal surface was recorded, including the edges and the centre of the basal (001) surfaces. Owing to inherent drift that occurs with long time in situ AFM measurements, we show well-equilibrated images of the surfaces over shorter timeframes. These are representative of the full experimental time wherein we monitored the surface evolution for >10 h, and in some cases exceeding 36 h, which is an extensive time for in situ AFM observations. All images were collected in contact mode; we verified that scanning in contact mode had no influence on the crystal's surface dissolution with increasing in the scan size at the end of each experiment and observing uniform changes across the entire scanned areas.

We measured the rate of drug release by measuring the negative step velocity v on the (001) surfaces. The displacement between step edges Δx were measured between sequential AFM height mode images. The time between images was recorded; therefore, we can quantify the step velocity as in equation (1):

$$v = \frac{\Delta x}{\Delta t} = \frac{x_2 - x_1}{t_2 - t_1} = \left[\frac{nm}{s}\right] \tag{1}$$

We quantify the drug release rate as proportional to the rate of molecules released for both F1 and F2. The rate of molecules n released is proportional to the integral of the velocity over time, equation (2):

$$n \propto l \int v \, dt \tag{2}$$

where $l = a = 0.54$ nm for F2, and the rate of molecules n released over time as shown by equation (3):

$$\frac{dn}{dt} = \rho v l = \left(\frac{\text{molecules}}{nm^2}\right)\left(\frac{nm}{s}\right)(nm) \tag{3}$$

where ρ is the density of molecules.

We measured >20 independent steps for each crystal size and crystalline form. From this, we determined the negative velocities and subsequently, the rate of molecules released. Error bars were for all molecules released for each crystal surface. The calculated rates of molecules released were summed to demonstrate the cumulative rate of drug release as a function of time in an undersaturated PBS solution such that different drug crystals were comparable.

We quantified the initial release of molecules from F1 crystals by measuring the trough profile of the dissolution at grain boundaries on the F1 crystal (001) surface. The troughs are triangular in habit; we selected a cross-sectional area wherein the sectional volume is that of a triangle. The initial release of molecules is therefore proportional to the number of molecules released from this area. To approximate this for F1, we used $l = \vec{a} \, \vec{c}$ where $\vec{a}$ and $\vec{c}$ lattice parameters (0.86 and 1.45 nm, respectively) to quantify the measured rate of release by the relationship in equation (1). For line measurements after the initial release, we used $l = \vec{c}$ based on the measured velocities in the $\vec{a}$ direction. The $\vec{c}$ direction corresponds to the single line width of the measured sectional area.

DSC and TGA. The analysis was conducted using the thermal analyser DSC 8000 (PerkinElmer). Studied samples were heated from 25 to 300 °C at 10 °C min⁻¹. Amorphous and crystal GW2580 (MII and MIII) samples were subjected to TGA under an inert nitrogen atmosphere to avoid undesired oxidation. The sample mass used in this study was 2–5 mg and a Pyris 1 TGA analyser (PerkinElmer) was utilized to follow mass changes in the studied samples, in response to temperature increase during the pyrolysis reaction where the thermogravimetric curves were obtained at heating rates of 1 °C min⁻¹ and heating between 50 and 400 °C.

SEM. Crystal size, morphology and topography were intensively studied with SEM. Samples were prepared for imaging by first placing them on conductive carbon paper and then coating with ~10 nm of gold/palladium (Au/Pd) using a Hummer 6.2 Sputter Coater System. Coated samples were imaged using the JEOL-JSM-5600LV scanning electron microscope with 2.0–15.0 KV acceleration voltage. For analysis purposes, three samples of each crystal preparation were studied as the following: three images were collected per sample and ten random measurements were applied per image.

Fabrication of alginate hydrogel spheres with or without drug. Alginate hydrogel spheres were made as reported previously[10]. Simply, a voltage generator was coupled to a syringe needle releasing alginate and grounded to a gelling

bath vessel. Spheres were produced from sterile alginate (PRONOVA SLG20, NovaMatrix), 2% w/v solution, dissolved in 0.9% saline (pH 7.4). For the drug formulation-loaded spheres, drugs crystals or amorphous drug (both amorphous methods) were added to the dissolved alginate and mixed well. We fabricated 500-µm-diameter alginate hydrogel spheres using a 23–25G blunt needle, 5–8 kV voltage and a flow rate of 200–300 µl min⁻¹. Blank alginate or with drug was then cross-linked in 250 ml gelling solution of sterile BaCl₂ (20 mM BaCl₂, 25 mM HEPES, 250 mM D-mannitol, pH 7.4). Following gelation, alginate spheres were washed four times with HEPES buffer (25 mM HEPES, 132 mM NaCl₂, 1.2 mM MgCl₂×6H₂O, 4.7 mM KCl, pH 7.4) and then four times with 0.9% saline, 40 ml each wash. Immediately following preparation, samples were implanted in vivo or tested in vitro to avoid any undesired self-crystallization (samples encapsulated amorphous drug) or initial drug release.

In vitro release from drug-loaded spheres (crystalline or amorphous). Release studies were carried out in different media depending on the studied drug. Curcumin: PBS (pH 7.4) + 20% ethanol or normal saline + 20% ethanol; QNZ: PBS + 10% DMF; GW2580: PBS and also under accelerated condition in PBS with SDS (0.1% or 0.3% w/v, as indicated). Sink condition was maintained across all of the in vitro-release studies. For curcumin- and QNZ-release studies, 100 µl of capsules loaded with 4 mg drug per ml were incubated in 2 and 3 ml release medium, respectively, at 37 °C. Sampling was done by total replacement of release media. Sampling timepoints were 10, 30 min, 1, 4, 16 h, 1, 2, 3, 5, 7, 10 and 14 d, and then weekly, until completion of a 60 d period. For release in accelerated condition (PBS + SDS), the same timepoints were followed while 20 µl of capsules with 10 mg drug per ml were incubated in 2 ml release medium to achieve sink conditions. Sample drug concentrations were quantified using an ultraviolet-calibrated system or through reversed-phase HPLC equipped with a C18 column. A gradient mode with a 1 ml min⁻¹ flow rate was applied and a different wavelength (nm) for each drug with 10–50 µl sample volumes being injected into an HPLC system (or ultraviolet-analysed Tecan infinite M200 PRO). Calibration curves, ranged over 0.05–500 µg ml⁻¹ (for most of the drugs, see below), and allowed for calculation of sample drug concentrations.

HPLC. Calibration curves were obtained on an Agilent 1100 Series HPLC instrument (Agilent Technologies) equipped with a binary pump (G1312A), autosampler (G1313A), degasser and photodiode detector (DAD, G1315A). Agilent ChemStation Software was utilized for HPLC system control, data acquisition and processing. The chromatographic separation was performed with an analytical Waters Atlantis T3 C18 column (5 µm, 4.6 × 250 mm). The temperature of the column and autosampler were kept at 20 °C. For all of the drugs, a gradient mode with a constant flow rate (1 ml min⁻¹) was applied using a mobile phase consisting of: (A) 0.1% formic acid (FA) in acetonitrile (ACN) and (B) 0.1% FA in water.

Stock solution of GW2580 (10 mg ml⁻¹) was prepared in DMSO and appropriate dilutions were made in DMSO to prepare standards (0.25–2,500 µg ml⁻¹) for the calibration curve of GW2580. Ten microlitres of standard solution was injected with analytes eluted by gradient mode. Mobile phase gradient conditions: (0 min 10% A), (10 min 95% A), (14 min 95% A), (16 min 10% A) and (20 min 10% A).

Stock solution of curcumin (10 mg ml⁻¹) was prepared in DMSO and appropriate dilutions were made in DMSO to prepare standards (0.05–500 µg ml⁻¹) for the calibration curve of curcumin. Ten microlitres of standard solution was injected with analytes eluted by gradient mode. Mobile phase gradient conditions: (0 min 70% A), (4 min 95% A), (10 min 95% A), (12 min 70% A) and (17 min 70% A).

Stock solution of QNZ (10 mg ml⁻¹) was prepared in DMSO and appropriate dilutions were made in DMSO to prepare standards (0.06–125 µg ml⁻¹) for the calibration curve of QNZ. Fifty microlitres of standard solution was injected with analytes eluted by gradient mode. Mobile phase gradient conditions: (0 min 20% A), (8 min 95% A), (12 min 95% A), (13 min 20% A) and (17 min 20% A).

Stock solution of LY2157299 (10 mg ml⁻¹) was prepared in DMSO and appropriate dilutions were made in DMSO to prepare standards (0.06–250 µg ml⁻¹) for the calibration curve of Ly2157299. Fifty microlitres of standard solution was injected with analytes eluted by gradient mode. Mobile phase gradient conditions: (0 min 10% A), (7 min 60% A), (8 min 95% A), (12 min 95% A), (13 min 10% A) and (17 min 10% A).

Stock solution of Ki20227 (10 mg ml⁻¹) was prepared in DMSO and appropriate dilutions were made in DMSO to prepare standards (0.06–500 µg ml⁻¹) for the calibration curve of Ki120227. Fifty microlitres of standard solution was injected with analytes eluted by gradient mode. Mobile phase gradient conditions: (0 min 20% A), (7 min 75% A), (8 min 95% A), (12 min 95% A), (13 min 20% A) and (17 min 20% A).

Stock solution of dexamethasone (10 mg ml⁻¹) was prepared in ethanol and appropriate dilutions were made in ethanol to prepare standards (0.06–500 µg ml⁻¹) for the calibration curve of dexamethasone. Fifty microlitres of standard solution was injected with analytes eluted by gradient mode. Mobile phase gradient conditions: (0 min 50% A), (7 min 80% A), (8 min 95% A), (12 min 95% A), (13 min 50% A) and (17 min 50% A).

Islet isolation, purification and encapsulation. Rat islets were derived from 300 g (8–10 week old) male Sprague–Dawley rats (Charles River) as previously

reported[12]. Isolation surgeries were conducted following a previously reported method[61]. Briefly, the bile duct was cannulated and the pancreas distended by an injection of 0.15% Liberase (Research Grade, Roche) in RPMI 1640 media. Until the completion of all surgeries, isolated pancreatic organs were kept on ice in conical tubes (50 ml). Following this, sample tubes were placed in a 37 °C water bath for 30 min digestions, and then stopped with addition of 10–15 ml cold M199 media (+10% HIFBS) with light shaking. Digested pancreases were then washed twice in M199/HIFBS media, filtered with a 450 μm sieve, and suspended in a Histopaque 1077 (Sigma)/M199 media gradient for centrifugation at 1,700 RCF at 4 °C. Depending on the gradient islet layer thickness, this step could be repeated for higher-purity islets. Finally, the islets were collected and further isolated through a series of six sedimentations (by gravity), with supernatant discarded after 4 min following each step. The purified islets were counted under light microscope and then washed three times in sterile PBS (×1). Samples were then washed once with RPMI 1640 (+10% HIFBS & 1% Pen/Strep), and then cultured in the same overnight for further use. For human islets, cells were purchased and obtained from ProdoLabs, in line with their rules for ethical sample procurement.

Just before encapsulation, the cultured islets were centrifuged for 1 min at 1,400 r.p.m. and then washed three times with Ca-free KREBS-Henseleit (KH) buffer (25 mM HEPES, 1.2 mM MgSO₄×7H₂O, 4.7 mM KCl, 135 mM NaCl, and 1.2 mM KH₂PO₄, pH 7.4). Afterwards, islets were centrifuged and all supernatant aspirated. The resulting islet pellet was resuspended in 2% w/v alginate solution (SLG20, in normal saline) with or without crystals for an islet density of 1,000 rat islets per ml alginate solution. For human islet preparations, cells were cultured as instructed by the vendor, and 3,000 were suspended per 1 ml alginate solution, with delivery of 2/3 of the total/mouse. Spheres were formed using BaCl₂ gelling solution and their sizes controlled as described above. Encapsulated islets were then immediately collected and washed six times with each HEPES buffer and normal saline, before transplantation. Due to variable islets size (50–400 μm), with some islet loss during encapsulation, total islet numbers were recounted following encapsulation and converted into islet equivalents as previously published[62]. For SC delivery, the capsules were placed in two separate but elongated SC locations, one on each side of the animal (Supplementary Fig. 18). Injection pockets were elongated by tunnelling away from the needle stick site and injecting capsules continuously as the needle was slowly withdrawn.

Implantation/transplantation surgeries. All animal surgeries and protocols were carried out in complete compliance with all relevant ethical regulations, as approved by the MIT Committee on Animal Care (IACUC). In addition, all surgical procedures as well as the post-operative care were supervised by the veterinary staff of MIT Division of Comparative Medicine. Implant and transplant procedures were carried out as previously described[10,12]. Namely, immune-competent 6- to 8-week-old, male STZ-induced diabetic or non-diabetic C57BL/6 mice (Jackson Laboratory) were anaesthetised with 3% isoflurane, and then their abdomens (or mid-backs) shaved and sterilized using betadine and isopropanol. All mice received 0.05 mg kg⁻¹ buprenorphine SC as a pre-surgical analgesic, plus 0.3 ml 0.9% NaCl (to prevent dehydration). Injections using 18-gauge needles were carried out for spheres or a 0.5 cm incision was made along the mid-back for discs for SC implantation. For IP implants, a 0.5–1.0 cm incision was used along the abdomen midline and the peritoneal wall following exposure by blunt dissection. Spheres (either with or without islets) were loaded into sterile pipette tip/needles for injection or PDMS discs (5 mm diameter and 2.2 mm thickness prepared following curing for 10 h at 45 °C of the SYLGARD 184 kit with ratio of 9:1 for elastomer base:curing agent, respectively, see Supplementary Fig. 19a) were placed for implantation into the peritoneal space. Then the peritoneal wall was closed with 5-0 polydioxanone (PDS II) bioabsorbable sutures. When appropriate, skin (for both IP and SC methods) was closed with wound clips and tissue glue.

For procedures in NHPs, buprenorphine (0.01–0.03 mg kg⁻¹) was preoperatively administered as an analgesic. NHPs were then sedated by IM ketamine (10 mg kg⁻¹) injection, with possible addition of midazolam by vet staff if needed. Animals were kept on circulating warm water-based blankets and covered during the entire procedure for body temperature maintenance. Both SLG20 0.5- or 1.5-mm-diameter spheres either no drug or drug-loaded were implanted IP by minimally invasive laparoscopic surgery, or injected SC into the dorsa and flanks of 4–6 kg, ~3- to 5-year old, cynomolgus macaque NHPs with 12- and 18-gauge sterile stainless steel needles custom-manufactured (Harvard Apparatus), as previously described[10,12]. Tangentially, the needles were inserted and ~1–2 cm were tunnelled away from the initial injection site, to separate the wound field from that of eventual material response. Spheres were injected into four total spots (for subsequent retrievals at timepoints specified below) with spheres either 0.5 or 1.5 mm in diameter, depending on the animal.

In all cases, experimental endpoints were chosen to balance initial goals of characterizing drug effects and therapeutic efficacy with later demonstrating remaining crystalline drug reservoirs over longer periods of time.

Blood glucose monitoring. C57BL/6 mice were treated with STZ by the vendor (Jackson Laboratory) before shipment to MIT to produce diabetic mice. Once received, blood glucose levels (BGs) of all mice were retested to confirm diabetic state before transplantation. Only mice with non-fasted BGs > 300 mg dl⁻¹ for two consecutive days were used.

BGs were measured twice a week after transplantation with capsules (with or without co-encapsulated drug formulation). One blood droplet was collected from the tail vein by lancet and tested using the Clarity Plus commercial glucometer (PN 20212-001, Clarity Diagnostics). Tested mice with unfasted BGs < 220 mg dl⁻¹ were considered cured (normoglycemic). BGs monitoring was continued until sample retrievals.

Retrieval of cells, tissues and materials. Procedures were carried out as previously described[10,12], and at timepoints as specified in figures. Briefly, mice were euthanized, and (in some instances) 5 ml of ice cold PBS was injected for IP lavages to collect IP immune cells. An incision was then made along the abdomen and peritoneal wall, and IP lavages were pipetted out into fresh falcon tubes (15 ml, each containing 5 ml RPMI media). Next, a spray bottle with KREBS buffer was used to rinse out all spheres in the abdomen into collection Petri dishes. Following this, ensuring all the spheres were retrieved (manually if need be; for example if fibrosed directly to IP tissues), samples were transferred into conical tubes (50 ml) on ice for downstream imaging and processing. Fibrosed IP capsules/tissues were also excised for FACS and expression studies. For SC samples, wide incisions were made in the skin for careful isolation of materials for post-retrieval analyses.

For NHP IP and SC retrievals, animal preparation for live excision procedures was carried out similar to times of implantation (described above). Then, biopsy punches (8 mm) were used to both sample the skin and SC space at two and four weeks and six months retrieval timepoints. Following the retrieval, sites were closed with 3-0 nylon sutures and tissue glue. For IP retrievals, minimally invasive laparoscopic surgery was also used (similar to implant procedures).

Imaging of the retrieved capsules. Phase-contrast and bright-field imaging of retrieved materials was carried out as previously described[10–12]. Samples were washed with KREBS buffer and transferred into Petri dishes (35 mm) for imaging using an EVOS microscope (Xl, Advanced Microscopy Group) for both phase-contrast and bright-field imaging.

Live/dead islet staining. Carried out as previously described[12]. A LIVE/DEAD Viability/Cytotoxicity kit (catalogue no. L-3224, Life Technologies) was used as specified by the manufacturer to assess islets viability post-encapsulation with and without co-encapsulated drug formulations.

Confocal immunofluorescence. Immunofluorescence imaging was carried out as previously described[10–12], and used to determine immune populations and fibrotic deposition on implant surfaces. Implants were retrieved from mice as described above and fixed overnight at 4 °C with 4% paraformaldehyde. Afterwards, samples were washed twice with KREBS, permeabilized for 30 min using 0.1% Triton (X100), and then blocked for 60 min with 1% bovine serum albumin (BSA). Next, the samples were stained for 60 min with a cocktail consisting of DAPI (500 nM) and marker probes (1:200 dilution in 1% BSA solution) as noted in displayed figures (antibodies listed under FACS analysis). Following staining, samples were washed three times with 0.1% Tween20 solution and kept in 50% glycerol. Samples imaged in glass-bottom plates using a confocal microscope (LSM700, Carl Zeiss Microscopy).

Histological processing. Retrieved samples were fixed overnight with 4% paraformaldehyde, at 4 °C. Tissue-embedded samples were then moved to 70% ethanol, while samples of free alginate spheres were moved directly to saline. Samples were then processed for paraffin embedding, sectioning and staining according to standard histological (Masson's trichrome or H&E).

Quantitative PCR analysis. As previously described[10], RNA was isolated from samples snap-frozen in liquid nitrogen immediately following excision, using the TRIzol protocol (Invitrogen). Given thorough sample homogenization, displayed gene expression signatures are representative of host response on and/or around retrieved implants. All samples were normalized by loading 1 μg total RNA in all cases for reverse transcription using the High Capacity cDNA Reverse Transcription kit (catalogue no. 4368814; Applied Biosystems). Complementary DNA (1:20 dilution) was amplified by quantitative PCR (qPCR) with the following primers: mouse α-SMact (5′-CGCTTCCGCTGCCCAGAGACT-3′; reverse: 5′-TATAGGTGGTTTCGTGGATGCCCGCT-3′), rat Pdx1 (5′-CTCTCG TGCCATGTGAACC-3′; reverse: 5′-TTCTCTAAATTGGTCCCAGGAA-3′), rat Cd68 (5′-GCCACAGTACAGTCTACCTTA-3′; reverse: 5′-AGAGATGAATTCT GCGCTGA-3′), rat α-SMact (5′-CGCTTCCGCTGCCCGGAGACC-3′; reverse: 5′-TATAGGTGGTTTCGTGGATGCCCGCC-3′) and rat TNF-α (5′-CACG CTCTTCTGTCTACTGAACTTC-3′; reverse: 5′-GAGTGTGAGGGTCTGGGC CATG-3′). Primers were designed with Primer Express (Applied Biosystems) and evaluated with LaserGene (DNAStar) to ensure species rat (encapsulated islet) or mouse (host) specificity. They were also normalized to either mouse (5′-GCT TCTTTGCAGCTCCTTCGTT-3′; reverse: 5′-CGGAGCCGGTTGTCGACGACC-3′) or rat (5′-ACCTTCTTGCAGCTCCTCCGTC-3′; reverse: 5′-CGGAGCCGTT GTCGACGACG-3′) β-actin, respectively. Samples were incubated for 10 min

at 95 °C followed by 40 cycles of 95 °C for 15 s and 60 °C for 60 s in a Roche 480 LightCycler. Results were analysed using the comparative C_T ($\Delta\Delta C_T$) method and are presented as relative RNA levels, to controls as specified in figure legends, after normalization to β-actin.

FACS analysis. As previously described[10], single-cell suspensions of freshly excised tissues and/or capsules were prepared using a gentle MACS Dissociator (Miltenyi Biotec). Sample suspensions were prepared in passive PEB dissociation buffer and passed through 70 µm filters (catalogue no. 22363548, Fisher Scientific) to remove debris. This procedure yielded the majority of cells adhered to implant surfaces (>90%). All tissue-derived samples were also subjected to red blood cell lysis with 5 ml of 1× RBC lysis buffer (catalogue no. 00-4333, eBioscience) for 5 min at 4 °C, with termination through the addition of 20 ml sterile PBS (1×). Remaining cells were centrifuged (300–400 g at 4 °C) and resuspended in 50 µl of eBioscience Staining Buffer (catalogue no. 00-4222) for staining in the dark for 25 min at 4 °C. Stains included monoclonal antibodies for CD11b (1 µl (0.2 µg) per sample; or CD11b-Alexa-488, Clone M1/70, catalogue no. 101217, BioLegend), Ly-6G (Gr-1) (1 µl (0.5 µg) per sample; Ly-6G-Alexa-647, Clone RB6-8C5, catalogue no. 108418, BioLegend) and CD68 (1 µl (0.5 µg) per sample; CD68-Alexa647, Clone FA-11, catalogue no. 11-5931, BioLegend). Two millilitres of stain buffer (catalogue no. 00-4222, eBioscience) was then used for three consecutive wash steps involving centrifugation for 5 min (400–500 g at 4 °C), with supernatants aspirating in between. Following all washes, samples were resuspended in 500 µl of Flow Cytometry Staining Buffer and run through a 40 µm filter (catalogue no. 22363547, Fisher Scientific) for eventual FACS analysis using a BD LSRII or Fortessa (BD Biosciences). Unstained, single antibody and immunoglobulin-G (labelled with either Alexa-488 or Alexa-647, BioLegend) controls were also used. For NHP cell staining, anti-human CD68 Alexa Fluor-647-conjugated antibody (Clone KP1, catalogue no. sc-20060) was used with the BioLegend (anti-mouse/human) CD11b-AF488 antibody (mentioned above).

NanoString analysis. RNAs for mock (saline) controls, or for various drug-loaded 0.5-mm-diameter alginate sphere-bearing mice ($n = 5$ per group) were isolated from described tissue samples, at various timepoints post-implantation. They were then quantified, diluted to the appropriate concentration, 100 ng µl⁻¹, with 5 µl of each sample processed according to manufacturer protocols for analysis with our customized multiplexed gene panels. NHP RNAs collected from samples retrieved over multiple months following implantation of crystal-formulated GW2580 were also analysed on a separate multiplexed primate gene expression array. Expression levels were obtained following nCounter (NanoString Technologies) quantification, with samples analysed using nSolver analysis software (NanoString Technologies). Housekeeping genes: *Cltc*, *Bact*, *Hprt1* and *Tubb5* were used to normalize, and data were log transformed.

LCMS and plasma samples. For this analysis, we used LC pumps of Agilent 1290 Infinity Binary pumps with a CTC Pal autosampler and MS of Sciex API6500 triple quad. Samples were stored at −80 °C until analysis. An extraction method, namely protein precipitation, was applied on the samples with a 10 µl sample processing extraction volume. For example, for GW2580 plasma concentration analysis, the following step-by-step sample extraction procedure was followed: (1) 10 µl of calibration standards and quality controls, blanks and samples were aliquoted into a 96-well plate; (2) 60 µl of IS-SS (internal standard) (100 ng ml⁻¹ QNZ, carbutamide, chrysin, carbamazepine, glafenine, dexamethasone, glyburide and d4AEA in ACN) were added to all samples except for double blanks, while 60 µl of ACN was then added to double blanks; (3) the plate was covered and samples mixed, followed by centrifugation for 5 min at ~3,000 r.p.m. at 4 °C; (4) by using a liquid plate, 50 µl of the supernatant was then transferred to a clean plate; (5) samples were diluted with 100 µl of MilliQ water, and the plate was once again covered and mixed for about 1 min before sample injection onto the LCMS/MS at 1.00–2,500 ng ml⁻¹. LC conditions: a C18 column (50 × 2.1 mm, 1.7 µm) of Waters BEH was used and the run temperature was 50 °C. Both mobile phase A (95.0:5.0:0.1 for water:ACN:FA (1.2 min)) and mobile phase B (50.0:50.0:0.1 for methanol:ACN:FA (1.3 min)) were used with 0.8 ml min⁻¹ as a flow rate and 2 µl as an injection volume. MS conditions: MS/MS: API-6500, with electrospray ionization method: positive ion, resolution: unit and source temperature of 550 °C. Transitions (m/z): compound ID: GW2580 367.0/245.1 Da. Int Std ID: QNZ 357.0/197.1 Da. Data analysis: regression type linear ($1/(x \times x)$), accepted curve range 0.50–2,500 ng ml⁻¹ and carryover 0.00%.

Cryogenic SEM. Images of 0.5 or 1.5 mm capsules loaded with drug crystals were taken using the Zeiss NVision 40 instrument (Carl Zeiss SMT) with the field emission SEM and 1–2 kV acceleration voltages. For sample preparation: 20–50 µl of spherical capsules were first transferred to a proper sample stub and then immersed into a slushy nitrogen bath (liquid and solid). Next, samples were placed in a vacuum cryo transfer system (EM VCT100, Leica Microsystems) where by controlled specimen sublimation surface water (ice) was removed in a selective manner. For cross-section images, frozen samples were fractured using a sharp blade. Lastly, before imaging, both fractured and unfractured spheres were coated with a thin layer of Pt/Pd with a sputter machine.

CGM coating. Enlite sensors (second generation) were coated with polyimide polymer with drug (that is GW2580 or dexamethasone) at 10% w/w or without, by painting the sensor tip using 29G needle to form a thin uniform layer. Crystals of small size crystals starting from 200 nm up to a few micrometres were used for this application and mixed well with the polyimide before applying onto the sensor tip. Coated sensors were incubated for 24 h at 40 °C for each coated side for full polyimide curing and solidifying. All sensors were sterilized under ultraviolet before implantation.

IVIS imaging. Subcutaneous evaluation of CGM inflammatory response was performed as described in Bratlie et al[63]. Each CGM (untreated and treated) was subcutaneously inserted into bilateral sites on the mid-back of female SKH1 mice, ~0.8 cm paramedian to the midline, as previously described[64]. Six days before SC insertion, mouse food was changed to special pellets with low fluorescence background (alfalfa free), and 100 µl of Prosense 750 was injected IP 16–24 h before the imaging time. Whole-body IVIS imaging was then performed, utilizing equivalent regions of interest for quantification of implant groups. Representative inflammation responses (from $n = 5$ mice in all cases) are shown in displayed images, along with quantification bar graphs (data: mean ± s.e.m) with (non-implant) background being subtracted.

CGM in vitro and in vivo functional testing. The in vitro glucose-sensing assay was performed with solutions at different glucose concentrations, as previously described[64]. Briefly, the solution was spiked every 15 min with a concentrated amount of glucose to bring the solution higher in 20 mg dl⁻¹ increments. The signal from two sensors in each case (that is, non-coated versus coated) was plotted as signal versus time, normalized and graphed.

For in vivo functional testing of the sensors, SKH1 mice were anaesthetised as previously described[64]. Drug-coated and control Medtronic MiniMed EnLite glucose sensors were inserted subcutaneously. A few minutes later, the sensor hydration period was completed, and then an iPro2 recording unit was plugged in for data recording.

BGs measurements in mice was started 1–2 h following sensor insertion in the mice, and the first BG reading was taken. BGs were taken often throughout each day for the first 3 d. BGs from blood droplets collected from the tail vein using a lancet (Medipoint) were measured using the Clarity Plus hand-held monitor (Clarity Plus, PN 20212-001, Clarity Diagnostics).

CGM recording data analysis started immediately once recording was completed, and the data were uploaded to the Medtronic CareLink iPro Therapy Management online portal. For calibration, all manually taken BG measurements were used. The Medtronic CareLink iPro online portal then calculated a 'glucose level' at each timepoint for the entire recording period, based off of the raw signal trends collected by the iPro recorders.

MSD and drug-coated MSD fabrication. The fabrication begins with a silicon wafer as the platform. Onto the bare silicon wafer, a thin layer of polyimide was spin coated onto the wafer. After curing the polymer base layer, nanoscale layers of gold (Au) and titanium (Ti) were deposited through electron beam deposition onto the polymer layer. Once the metal electrode layers were deposited, standard photolithography techniques were used for the Peano curve design; the wafer was exposed to ultraviolet light through a photomask and then selectively etched to produce the pattern. To encapsulate the patterned metal traces another polyimide layer was applied, spin coated on and cured. Then, a layer of aluminium (Al) was deposited to act as a protective layer for the polymer during further etching. This aluminium was then selectively etched and open electrode contact points were produced through photolithography and reactive ion etching. Finally, the MSDs were detached from the wafer using acetone and wired using Kapton polyimide tape interconnects. For fabrication of drug-coated MSDs (and control) an extra layer for each side surface was applied and coated with polyimide polymer with drug (that is, GW2580) at 10% w/w or without, by painting the device side using 29G needle to form a thin uniform layer. Crystals of small size crystals starting from 200 nm up to few micrometres were used for this application and mixed well with the polyimide before applying onto the device surface. Coated devices were incubated for 24 h at 40 °C for each coated side, plus as needed an extra 24 h at the same conditions for full polyimide curing and solidifying.

MSD in vivo evaluation. All devices were sterilized under ultraviolet light before implantation. Pre-emptive analgesia was administered subcutaneously at the following doses: buprenex (0.03 mg kg⁻¹) and meloxicam (1.0 mg kg⁻¹). All surgical procedures were carried out under isoflurane (2.0%)/oxygen inhalation. The surgical site was shaven with an electrical clipper and the exposed skin was cleansed with several cycles of betadine scrub followed by isopropanol rinse. All surgeries were performed using aseptic technique. A 1–2 cm incision was made parallel to the femur, and blunt dissection was performed through the vastus lateralis and biceps femoris muscle plains to reveal the sciatic nerve. This nerve was traced down towards the knee until the individual branches (peroneal, sural and tibial) were revealed at the level of popliteal fossa. The tibial nerve was identified as the largest and most central branch. By using micro-dissecting scissors and ultrafine forceps, the tibial nerve was separated from the peroneal

and sural nerve branches and carefully cut as distally as possible as via micro-dissecting scissors, thus avoiding the popliteal vessels. The device was sutured securely to the gastrocnemius using four polyprolene sutures. The wires of the device were tunnelled subcutaneously up dorsally to reach the incision made at the scalp. Headstages, connected to the end of the wire bundle, were mounted on the skull using dental ceramic. The animals were monitored until consciousness was regained. Post-operative checks were done 14 h after surgery. Buprenex (0.03 mg kg^{-1}) was administered at 8 h intervals for post-surgical pain management. Meloxicam (1.0 mg kg^{-1}) was administered every 24 h for 48 h.

Stimulating procedure. Using the Arduino IDE, we were able to pre-programme the desired parameters for functional electrical stimulation and upload it to the rfDuino microcontroller. The system then draws the necessary current out of the low-power coin battery at the set programmed intervals and outputs it to the MSD. The rfDuino is wired to the MSD using thin medical-grade stranded stainless steel wire (CoonerWire AS633). The current travels through the MSD and out of the small contact pads where it interfaces with tissue. We sought to determine the therapeutic effects of muscle stimulation using the MSD device for prevention of atrophy during peripheral nerve injury. Five MSD devices, both drug coated and uncoated, were implanted along the surface of the gastrocnemius muscles of Lewis rats after resection of the tibial nerves. After surgical implantation, the animals were given 3 d of post-op before initiation of the stimulation regimen. The animals were stimulated with 500 mV, 2 Hz of functional electrical stimulation (FES) for an hour a day, five days a week for two weeks. Afterwards, the gastrocnemius muscles were collected for histological analysis.

Muscle fibre atrophy quantification. Axial slices of the gastrocnemius muscle tissue where the device was implanted were analysed. These slides were stained with H&E and used to quantify muscle fibre area. The slides were scanned and digital images were opened on ImageJ software to measure. The area of muscle fibres can be a good indication of atrophy as muscles tend to decrease in size when not being used. Using the polygon tool and 'measure' function, muscle fibres were outlined, measured and recorded. Multiple images of each slide were taken and at least 200 fibres from each slide were measured. Average muscle fibre areas of the experimental and control groups were calculated and compared with one another.

Statistics and reproducibility. All line and bar graph data are expressed as mean ± s.e.m, with $N = 5$ mice per timepoint and per treatment group. The sample sizes where chosen based on previous literature as well as to ensure statistical power in determining data significance. The number of times each experiment was independently repeated is listed in each figure legend. Panels are representative of similar results across experimental repeats. All animals were included except in instances of unforeseen morbidity. Animal cohorts were also randomly selected.

Investigators were not blinded to experiments as blinding was not possible for part of the data analysis, especially in vitro, due to visual observations of deposited crystalline drug (that is, having different shading or colours, drug depending) identifying drug-containing treatment groups. For FACS or qPCR, data were analysed for statistical significance either by one-way analysis of variance (ANOVA) with Bonferroni multiple comparison correction or unpaired, two-tailed t-test, unless otherwise indicated, as implemented in GraphPad Prism 7; $*P < 0.05$; $**P < 0.001$; $***P < 0.0001$. High-throughput NanoString-based gene expression data were normalized using the geometric means of the positive controls, with background levels established using the means of the negative controls.

Ethical compliance. We confirm that we have complied with all relevant ethical regulations, as specified in further detail in the Methods.

Reporting Summary. Further information on research design is available in the Nature Research Reporting Summary linked to this article.

Data availability
The data supporting the findings of this study are available within the article and its supplementary information files and from the corresponding author upon reasonable request.

References
56. SAINT (Bruker AXS, 2011).
57. Krause, L., Herbst-Irmer, R., Sheldrick, G. M. & Stalke, D. Comparison of silver and molybdenum microfocus X-ray sources for single-crystal structure determination. *J. Appl. Crystallogr.* **48**, 3–10 (2015).
58. Sheldrick, G. M. SHELXT—integrated space-group and crystal-structure determination. *Acta Crystallogr. A* **71**, 3–8 (2015).
59. Sheldrick, G. M. Crystal structure refinement with SHELXL. *Acta Crystallogr. C* **71**, 3–8 (2015).
60. Müller, P. Practical suggestions for better crystal structures. *Crystallogr. Rev.* **15**, 57–83 (2009).
61. Lacy, P. E. & Kostianovsky, M. Method for the isolation of intact islets of Langerhans from the rat pancreas. *Diabetes* **16**, 35–39 (1967).
62. Ricordi, C. et al. Islet isolation assessment in man and large animals. *Acta Diabetol. Lat.* **27**, 185–195 (1990).
63. Bratlie, K. M. et al. Rapid biocompatibility analysis of materials via in vivo fluorescence imaging of mouse models. *PLoS ONE* **5**, e10032 (2010).
64. Xie, X. et al. Reduction of measurement noise in a continuous glucose monitor by coating the sensor with a zwitterionic polymer. *Nat. Biomed. Eng.* **2**, 894–906 (2018).

Corresponding author(s): Daniel G. Anderson

Reporting Summary

Nature Research wishes to improve the reproducibility of the work that we publish. This form provides structure for consistency and transparency in reporting. For further information on Nature Research policies, see Authors & Referees and the Editorial Policy Checklist.

Statistical parameters

When statistical analyses are reported, confirm that the following items are present in the relevant location (e.g. figure legend, table legend, main text, or Methods section).

n/a	Confirmed	
☐	☒	The exact sample size (*n*) for each experimental group/condition, given as a discrete number and unit of measurement
☐	☒	An indication of whether measurements were taken from distinct samples or whether the same sample was measured repeatedly
☐	☒	The statistical test(s) used AND whether they are one- or two-sided *Only common tests should be described solely by name; describe more complex techniques in the Methods section.*
☒	☐	A description of all covariates tested
☐	☒	A description of any assumptions or corrections, such as tests of normality and adjustment for multiple comparisons
☐	☒	A full description of the statistics including central tendency (e.g. means) or other basic estimates (e.g. regression coefficient) AND variation (e.g. standard deviation) or associated estimates of uncertainty (e.g. confidence intervals)
☐	☒	For null hypothesis testing, the test statistic (e.g. *F*, *t*, *r*) with confidence intervals, effect sizes, degrees of freedom and *P* value noted *Give P values as exact values whenever suitable.*
☒	☐	For Bayesian analysis, information on the choice of priors and Markov chain Monte Carlo settings
☒	☐	For hierarchical and complex designs, identification of the appropriate level for tests and full reporting of outcomes
☒	☐	Estimates of effect sizes (e.g. Cohen's *d*, Pearson's *r*), indicating how they were calculated
☐	☒	Clearly defined error bars *State explicitly what error bars represent (e.g. SD, SE, CI)*

Our web collection on statistics for biologists may be useful.

Software and code

Policy information about availability of computer code

Data collection	All commercial software suites are specified. No custom software code was used. Briefly: 1) Agilent ChemStation Software (Agilent 1100 Series) 2) nSolver analysis software (NanoString Technologies Inc., Seattle, WA) 3) ImageJ software 4) The programs SAINT, SHELXT and SADABS For XRD (reference was given in the paper) 5) GraphPad Prism 7
Data analysis	All commercial software suites are specified. No custom software code was used. The same above softwares were also used for data collection and analysis. A detailed description on how many times samples were analyzed, number of measurements per sample/or image, unit of measurement, and how the data was analyzed all given in details for each software.

For manuscripts utilizing custom algorithms or software that are central to the research but not yet described in published literature, software must be made available to editors/reviewers upon request. We strongly encourage code deposition in a community repository (e.g. GitHub). See the Nature Research guidelines for submitting code & software for further information.

Data

All manuscripts must include a [data availability statement](#). This statement should provide the following information, where applicable:

- Accession codes, unique identifiers, or web links for publicly available datasets
- A list of figures that have associated raw data
- A description of any restrictions on data availability

Data supporting the findings of this study are available within the article [and its supplementary information files] and from the corresponding author upon reasonable request.

Field-specific reporting

Please select the best fit for your research. If you are not sure, read the appropriate sections before making your selection.

☒ Life sciences   ☐ Behavioural & social sciences   ☐ Ecological, evolutionary & environmental sciences

For a reference copy of the document with all sections, see [nature.com/authors/policies/ReportingSummary-flat.pdf](#)

Life sciences study design

All studies must disclose on these points even when the disclosure is negative.

Sample size	No sample size calculation was performed. Instead, we relied on journal guidelines for a minimum of n = 5 animals/treatment group, except with the non-human primate study where animals were limited. Numbers in this case are also clearly reported in the Figure Legends. In addition, we adhered to sample size requirements necessary for determining statistical significance as well as reproducible therapeutic effect.
Data exclusions	No data was excluded from analyses.
Replication	All attempts at replication were successful. Experimental repeat numbers are also reported in Figure Legends. A reproducibility statement has also now been added to the Statistical Analysis and Reproducibility section.
Randomization	Animal groups were randomized by body weight and/or the level of their diabetic state (ie., blood glucose status following fasting and prior to transplantation).
Blinding	Blinding was not possible for part of the data analysis, especially in vitro, due to visual observations of deposited crystalline drug (ie., having different shading or colors, drug-depending) identifying drug-containing treatment groups. However, with that said, those on the biology/immunology side were generally blinded from more of the mainstream chemistry analyses, and vice versa.

Reporting for specific materials, systems and methods

Materials & experimental systems

n/a	Involved in the study
☐	☒ Unique biological materials
☐	☒ Antibodies
☐	☒ Eukaryotic cell lines
☒	☐ Palaeontology
☐	☒ Animals and other organisms
☒	☐ Human research participants

Methods

n/a	Involved in the study
☒	☐ ChIP-seq
☐	☒ Flow cytometry
☒	☐ MRI-based neuroimaging

Unique biological materials

Obtaining unique materials	All unique biological materials are readily available from standard commercial sources.

Antibodies

Antibodies used	The antibodies (Fluor-conjugated anti-mouse Ly-6G/Ly-6C (Gr-1), CD11b, and CD68) were purchased from BioLegend (San Diego, CA) and used as described below. For non-human primates immunostaining, anti-human CD68 antibody Alexa Fluor-conjugated was purchased from Santa Cruz (Dallas, TX). The CD11b (anti-mouse/human) antibody (from BioLegend-San Diego, CA) was used the same for both mouse and primate staining. The 425-600 μm acid washed glass spheres (Cat#/Lot#: G8772/SLBL7288V) and Cy3-conjugated anti-mouse α-SMact antibody were purchased from Sigma-Aldrich (St. Louis, MO). All antibody clone numbers and dilutions are included in the "FACS Analysis" Methods writeup.
Validation	All antibodies have been used by us as previously described for both rodent as well as non-human primate cells and tissues (refs10, 11, and 12). In addition, many have other literature references and species-specificity clearly denoted on their respective websites. In the case of the anti-CD68 KP1 Santa Cruz antibody, it was marked as anti-human, and we tested it against our previous non-human primate samples to validate it's efficacy in this monkey species (cynomolgus macaque) and model.

Eukaryotic cell lines

Policy information about cell lines

Cell line source(s)	ATCC
Authentication	Certification from vendor.
Mycoplasma contamination	RAW264.7 cells utilized in this study were tested in-house (Lonza MycoAlert kit) and shown to be negative for mycoplasma.
Commonly misidentified lines (See ICLAC register)	N/A. This is not a problem associated with this cell line.

Animals and other organisms

Policy information about studies involving animals; ARRIVE guidelines recommended for reporting animal research

Laboratory animals	As reported in the Methods section, animals used were: Male Sprague-Dawley rats (Body weights: all ~300 grams, 8-10 weeks), male C57BL/6 mice (healthy and STZ-induced diabetic) 8-12 week old, and non-human primate female cynomolgus monkeys (body weights: 4-6 kg) ~3-5 year old.
Wild animals	The study did not involve wild animals.
Field-collected samples	The samples did not involve samples collected from the field.

Flow Cytometry

Plots

Confirm that:

☒ The axis labels state the marker and fluorochrome used (e.g. CD4-FITC).

☒ The axis scales are clearly visible. Include numbers along axes only for bottom left plot of group (a 'group' is an analysis of identical markers).

☒ All plots are contour plots with outliers or pseudocolor plots.

☒ A numerical value for number of cells or percentage (with statistics) is provided.

Methodology

Sample preparation	As described in the Methods section in detail, this methodology to obtain single cell suspensions (despite having different implant devices and novel technology development in this study) is as also previously optimized and published in Doloff et al., 2017 Nature Materials (Main REF#10).
Instrument	Listed in the Methods section: BD FACSCalibur (cat. #342975), BD Biosciences, San Jose, CA, USA)
Software	Collection: Cell and for analysis: FloJo.
Cell population abundance	Sorting was not done. However, for FACS gating analysis: cell populations of interest (ie., macrophages) were incredibly abundant as main responders to material implant systems, reaching as much as 50 to 70% of the dissociated tissue or fibrotic capsule on implant surfaces. With that said, percentages and abundance (cell numbers) decreased significantly due to inclusion of crystalline drug formulations, as reflected in the study Figures.
Gating strategy	Again, the macrophage gating strategy was the same as previously optimized and published in Doloff et al., 2017 Nature Materials (Main REF#10). As a consequence, all flow cytometry data in the present study is shown exclusively as quantified bar graphs with error bars reflecting data spread, along with symbols reflecting the degree of statistical significance. As such, while

the next box on this form is checked, we would ask that our previous 2017 Nature Materials study be referred to for reference figures exemplifying gating strategy.

☒ Tick this box to confirm that a figure exemplifying the gating strategy is provided in the Supplementary Information.